Unified Modeling and Full-Mode Energy Control of Two-Time-Scale Cascaded Systems

Kai He, *Graduate Student Member, IEEE*, Fei Gao, *Member, IEEE*, Ying Jiang, Xijun Yang, *Member, IEEE*, and Hongchen Liu, *Senior Member, IEEE*

***Abstract*—Periodic energy control has been successfully applied to systems with single-time-scale operation. However, the control performance is hindered by the different time scales of the non-fully decoupled cascaded structure. In this article, a unified full-mode energy model with two-time-scale variables for the *LCC-LCC* compensated inductive power transfer (IPT) system with a rear-end four-switch buck-boost converter, which can accurately track the dynamic response, is proposed. To reduce the computational burden and improve the dynamic response speed, a full-mode energy control strategy conducting in the unified time scale is developed based on the two-time-scale model. Compared with the periodic energy control, the sampling of the load voltage and current can be avoided. A cascaded *LCC-LCC* compensated IPT-FSBB prototype is built, and the theoretical analysis shows excellent agreement with both the simulation and experimental results.**

***Index Terms*—Four-switch buck-boost (FSBB), full-mode energy control, inductive power transfer (IPT), multiple time scales.**

I. INTRODUCTION

A. Background

THE inductive power transfer (IPT) technology, as an alternative to cabled charging, has been used in many scenarios, such as autonomous underwater vehicles [1], uncrewed aerial vehicles [2], and electric vehicles [3]. As shown in Fig. 1, a four-switch buck-boost (FSBB) converter consists of power switches $S_1 \sim S_4$ and inductor L. D_1 and D_2 are the duty cycles of the two switching legs and α is the phase shift angle between the two duty cycles. Compared with the conventional buck and boost converters, there exists three degrees of control freedom in the FSBB converter, i.e., the duty cycles D_1 and D_2 of the two switching legs and the phase shift angle α between the two duty cycles. Additionally, different from the buck–boost converter, the output voltage polarity is the same as the input. Because of the voltage step-up/down ability, it is usually used as a rear-end converter to match the voltage levels required by different battery energy storage systems [4]. Besides, the FSBB converter often acts as the load impedance matching converter to achieve the maximum efficiency operation of the first-stage IPT system [5].

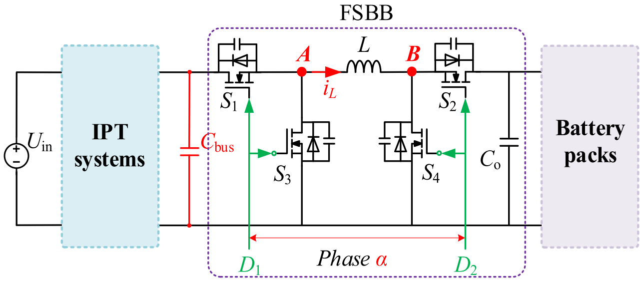

Fig. 1. Typical structure of the cascaded IPT-FSBB system under study.

Electrolytic capacitors are commonly used for decoupling the two cascaded stages. However, they have a relatively short lifespan, typically ranging from a few thousand hours [6]. Moreover, in high-power transfer systems, increased operating temperatures can further shorten the lifespan of these capacitors, causing their capacitance to deviate from the nominal value [7]. As the capacitance of electrolytic capacitors diminishes, maintaining a constant bus voltage becomes challenging, resulting in significant voltage ripples. Moreover, the frequencies of the compensation network and the rear-end converter are often different, therefore, the two-stage cascaded system cannot be considered fully decoupled. The assumptions underlying traditional modeling methods are no longer applicable. As shown in Fig. 2, the cascaded system contains the variables at multiple time scales, more generally, those systems can be called "singularly perturbed systems."

B. Literature Review and Motivation

The chief purpose of the singular perturbed approach to analysis and design is the alleviation of the high dimensionality and ill conditioning resulting from the interaction of slow and fast variables. Generalized state-space averaging (GSSA) [8] method is commonly used to model the IPT systems due to its good

Received 21 February 2025; revised 25 June 2025; accepted 24 July 2025. Date of publication 30 July 2025; date of current version 8 September 2025. This work was supported in part by the National Natural Science Foundation of China under Grant 52377194 and Grant 52307012 and in part by Shanghai Jiao Tong University Deep Blue Program under Grant SL2022MS009. Recommended for publication by Associate Editor M. S. ElMoursi. *(Corresponding author: Fei Gao.)*

Kai He, Fei Gao, and Xijun Yang are with the State Key Laboratory of Submarine Geoscience, Shanghai Jiao Tong University, Shanghai 200240, China, and also with the Key Laboratory of Control of Power Transmission and Conversion, Ministry of Education, School of Electrical Engineering, Shanghai Jiao Tong University, Shanghai 200240, China (e-mail: hk_3823@sjtu.edu.cn; fei.gao@sjtu.edu.cn; yangxijun@sjtu.edu.cn).

Ying Jiang is with the School of Electrical Engineering, Shanghai Dianji University, Shanghai 201306, China (e-mail: jiangy@sdju.edu.cn).

Hongchen Liu is with the School of Electrical Engineering and Automation, Harbin Institute of Technology, Harbin 150001, China (e-mail: fenmiao@hit.edu.cn).

Color versions of one or more figures in this article are available at https://doi.org/10.1109/TPEL.2025.3594025.

Digital Object Identifier 10.1109/TPEL.2025.3594025

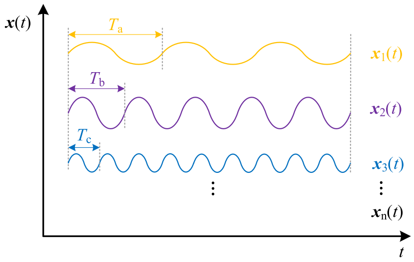

Fig. 2. Multi-time-scale variables existing in the cascaded system.

reflection of system dynamic characteristics, where the Fourier series is used to represent the state variables and the high-order characteristics are ignored. In [9], the effect of the switching ripple interaction of the cascaded converter is studied based on the impedance-based model, and an adaptive modulation sample-and-hold method is proposed to eliminate the effect of the switching ripple interaction. Similarly, a generic small-signal model of the triple-stage cascaded dc system is established in [10]. It is revealed that the whole system could be unstable even if the subsystem is stable. Considering the time-scale separation, the reduced-order model of the IPT system with a Cuk-based bridgeless rectifier on the secondary side is derived in singular perturbation form in [11]. Coupled mode theory [12], [13] can reduce the order of models with the help of variable substitution and linear transformation of GSSA. However, the presumptions on which the model is based will limited the simplicity, and due to variable transformations, the model does not intuitively reflect the physical characteristics of the system. Parity-time symmetry [14], [15] also has limitations due to its strict conditions of the resonant network of IPT system.

In the multi-time-scale cascaded system, the voltage ripple of the bus capacitor should be considered for accurate modeling. Besides, time-scale separation is the key catachrestic of the singular perturbation circuit system [16]. Although the aforementioned literature has conducted some analysis on the modeling of the cascaded system, the problems of high order caused by the compensation network of the IPT system and obtaining analytical solution are still challenging. Moreover, most of the aforementioned research is based on the operating modes of the system and the computational burden will inevitably increases due to the full-mode operation in the multiple time scales.

For the cascaded system, many studies concentrate on optimizing the performances of the system according to the different control goals. In [17], to pursue the fast-dynamic response, the model predictive control is applied to the dynamic IPT system with multiple controllable transmitters and a buck converter on the secondary side. In [18], a self-learning composite compensation control is studied for the two-time-scale systems, where the critic-only reinforcement learning and H_∞ control is employed for controller design. In [11], with the help of time-scale separation, the closed-loop control strategy with two loops for the cascaded IPT-Cuk system is studied to simplify the design process. In [19], the virtual impedance control with an auxiliary circuit is developed to improve the stability of the cascaded boost-boost converter. Phase-shift control [20], model predictive control [21], and input voltage control [22] are also studied by researchers for better performances of the cascaded system.

In practice, the control strategies are vulnerable to parameter identification errors [23], which also determine the accuracy of the system model. Periodic energy control of the single-stage IPT system is studied in [24] to reduce the sensitivity of the control variable to mutual inductance. However, to our best knowledge, there is a lack of research focusing on the energy control in cascaded systems, and models covering the dynamics of the cascaded system in multiple time scales are not presented.

C. Main Contribution

For the multitime-scale cascaded system, the simple energy control is preferred to capture the dynamics in the full-mode operation. To this end, this article develops a full-mode energy model by taking the two-time-scale cascaded IPT-FSBB system under nonfully decoupled condition as an example, which simplifies the derivation process compared with the existing modeling methods. Besides, the energy control strategy conducted in the full-mode period is proposed to overcome the obstacle caused by two-time-scale operation and periodic energy control.

The main contributions of this article are as follows.

1) The criteria for determining the unified time scale are provided, based on which an energy model for the two-time-scale IPT-FSBB system is developed in this article, which can accurately track the dynamic response of system outputs and features high accuracy and low complexity.
2) A composite full-mode energy control strategy conducted in the unified time scale is proposed, which overcome the time scale interaction and necessity of time-scale separation. Besides, the need for sampling load voltage and current, which significantly decreases the complexity of the hardware circuit design and the computational burden of the controller.
3) A small-signal model in the full-mode operating period of the cascaded IPT-FSBB system is developed, and the closed-loop characteristic of the energy control is analyzed.

D. Outline of the Article

The rest of the article is organized as follows. In Section II, the full-mode operation and principle of the port energy transfer of the IPT-FSBB system with two-time-scale operation, and the limitations of the single-time-scale energy model is presented. In Section III, the criteria for determining the unified time scale and the derivation of the two-time-scale energy model are proposed. The full-mode energy control and closed-loop characteristic is analyzed in Section IV. The effectiveness of the theoretical analysis is verified by experiments in Section V. Finally, Section VI concludes the article.

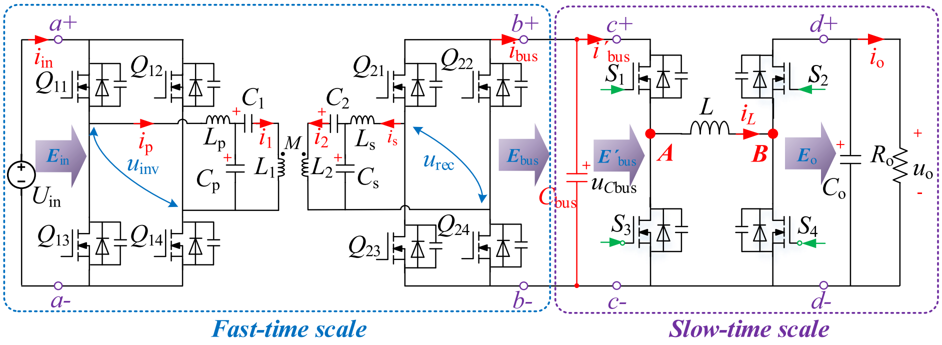

Fig. 3. Diagram of the two-time-scale IPT-FSBB system.

II. STUDY OBJECT

A. Two-Time-Scale Operation

The *LCC-LCC* compensated IPT system with a rear-end FSBB converter, which features high-order and multi-variable characteristics, is taken as an example for analysis in this article, as shown in Fig. 3. The active bridges on the primary and secondary sides consist of power switches $Q_{11}\sim Q_{14}$ and $Q_{21}\sim Q_{24}$, respectively. L_1 and L_2 are the coil inductances of the transmitting and receiving coils. M is the mutual inductance between the two coils and expressed as $k(L_1L_2)^{1/2}$, where k is the coupling coefficient. L_p, C_p, C_1 and L_s, C_s, C_2 are the compensation inductors and capacitors, respectively. The voltage gain of the rear-end FSBB converter is defined as $\sigma = D_1/D_2$ ($\sigma > 1$, boost mode. $\sigma = 1$, equal mode. $\sigma < 1$, buck mode).

The operating frequencies of the front-end IPT system and the rear-end FSBB converter are defined as $f_M = 1/T_M$ and $f_N = 1/T_N$, respectively. It can be seen from Fig. 3 that there exists two time scales in the cascaded IPT-FSBB system due to the different operating frequencies, i.e., the fast time scale f_M and the slow time scale f_N. The system can be modeled by

$$\begin{aligned}\dot{\boldsymbol{x}} &= f\left(x,z,t,\varepsilon\right), \mathrm{x}\left(t_0\right) = x^0\\ \varepsilon\dot{\boldsymbol{z}} &= g\left(x,z,t,\varepsilon\right), \mathrm{z}\left(t_0\right) = z^0\end{aligned} \tag{1}$$

where the m-dimensional vector $\boldsymbol{x} = [i_p\ u_{Cp}\ u_{C1}\ i_1\ i_2\ u_{C2}\ u_{Cs}\ i_s]^T$ is predominantly fast and the n-vector $\boldsymbol{z} = [C_{\text{bus}}\ i_L\ u_{Co}]^T$ contains slow transients superimposed on a fast varying "quasi-steady-state", that is $\|\ \dot{\boldsymbol{x}}\ \| \gg \|\ \dot{\boldsymbol{z}}\ \|$. In this article, $m = 8$ and $n = 3$. The scaling parameter ε is the speed ratio of the fast versus slow phenomena, which means that $\varepsilon = f_M/f_N = T_N/T_M$.

B. Principle of Energy Transfer

To simplify the analysis, the dead time of the power switches, the equivalent series resistances of the passive components, and the switching losses are neglected. In the perspective of energy transmission, as shown in Fig. 3, the input energy E_{in} of port ($a+$, a-) is generated by the dc source U_{in}, which can be expressed as

$$E_{\text{in}} = \int_t^{t+T_M} u_{\text{inv}}\left(\tau\right) i_p\left(\tau\right) d\tau. \tag{2}$$

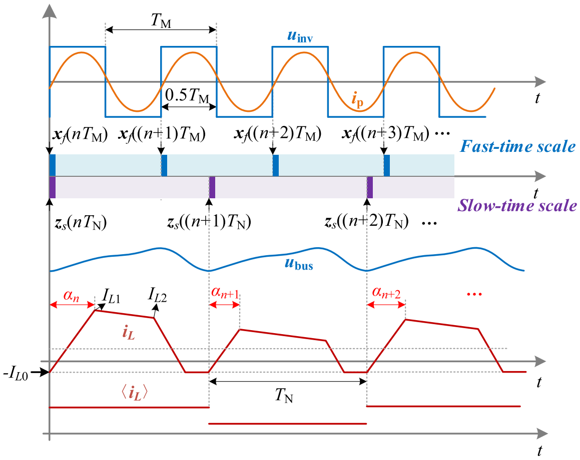

Fig. 4. Key waveforms of the two-time-scale operation when $\sigma > 1$.

Through the primary-side inverter, compensation network, coupling coils, secondary-side rectifier, and the bus capacitor C_{bus}, the energy is injected into the rear-end FSBB converter. The output energy of ports ($b+$, b-) and ($c+$, c-) are denoted by E_{bus} and E'_{bus}, respectively. It should be noted that $E_{\text{bus}} > E'_{\text{bus}}$ under non-fully decoupled operation, and

$$\begin{aligned}\Delta E_{\text{bus}} = E_{\text{bus}} - E'_{\text{bus}} &\int_t^{t+T_M} u_{C_{\text{bus}}}\left(\tau\right) i_{\text{bus}}\left(\tau\right) d\tau\\ &- \int_t^{t+T_N} u_{C_{\text{bus}}}\left(\tau\right) i\prime_{\text{bus}}\left(\tau\right) d\tau.\end{aligned} \tag{3}$$

In (3), the intervals of integration for E_{bus} and E'_{bus} are (t, $t+T_M$) and (t, $t+T_N$), respectively, which means that the operating frequencies of i_{bus} and i'_{bus} are different. Then, the output energy of port ($d+$, d-) is noted as E_o, which is consumed by the load R_o and can be calculated by

$$E_o = \int_t^{t+T_N} u_o\left(\tau\right) i_o\left(\tau\right) d\tau. \tag{4}$$

C. Limitations of the Single-Time-Scale Energy Model

Fig. 4 shows the time series diagram of the two-time-scale operation, where $\boldsymbol{x}_f$ and $\boldsymbol{z}_s$ represent the fast and slow sampling instants. $\boldsymbol{x}_f(nT_M)$ and $z_s(nT_M)$ are the coincident sampling instant. In the single-time-scale energy model, the cascaded system is considered to be decoupled and the bus voltage is constant. However, when the operating frequencies of the two stages are different and the capacitor voltage ripple rate ΔVCf exceeds 5% in the full-power range, there will exist two time scales for energy model derivation. It can be seen from (3) that the output energy of ports (b+, b-) and (c+, c-) need to be calculated in fast and slow periods T_M and T_N, respectively. It means that, under conditions of incomplete decoupling, at least two different sampling frequencies are required to calculate E_{bus} and E'_{bus} (i.e., the sampling values $\boldsymbol{x}_f(nT_{\text{M}})$, $\boldsymbol{x}_f((n{+}1)T_{\text{M}})$, $\boldsymbol{x}_f((n{+}2)T_{\text{M}})$, …, of $u_{C\text{bus}}$ and i_{bus}, and $z_s(nT_M)$, $z_s((n{+}1)T_N)$, $z_s((n{+}2)T_N)$, …, of $u_{C\text{bus}}$ and i'_{bus}), which significantly increases the computational burden on the digital controller. In other words, two sets of sampling circuits need to be designed for the variable $u_{C\text{bus}}$, resulting in an increase in hardware costs. In addition, for systems with two time scales, if the single-time-scale models are used separately, the synchronization issue between the two-stage system will also be one of the challenges in implementing energy control.

Moreover, as shown in Fig. 4, when the hybrid pseudo-continuous conduction mode (PCCM) zero-voltage-switching (ZVS) modulation scheme [25] is used in the IPT-FSBB system, the phase-shift α_n between the two legs of the rear-end FSBB converter changes with the required output power P_o, which means that there will be variations in the average current $\langle i_L \rangle$. $\langle i_L \rangle$ can be obtained by

$$\langle i_L \rangle_{T_N} = \frac{1}{T_N} \int_{nT_N}^{(n+1)T_N} i_L(t)\, dt. \tag{5}$$

Based on the analysis in [24] and [25], the optimal solution of the energy control demands that the sampling instants of variables are typified by the unified time scale. However, only the behaviors of u_A and u_B (see Fig. 3) in periodic time instants nT_N are considered, which results in the model's inability to precisely capture the variations in $\langle i_L \rangle$ that are induced by changes of phase-shift α_n during one operating period T_N. Thus, it brings challenges to the effective application of the energy model in the cascaded systems with two time scales.

III. TWO-TIME-SCALE ENERGY MODEL

A. *Time-Scale Unification*

Fig. 5 shows the time-scale unification diagram of the two time scales. Different from the decomposition method [27], where the fast process are neglect and the slow process $z_s(nT_N) = z_s((n{+}1)T_N) = z_s((n{+}2)T_N) = \ldots$, the purpose of the time-scale unification is to overcome the challenge of simultaneously calculating the port energy for two different time scales in (3) and to provide the unified model for composite energy control. It can be seen from Fig. 5 that the fast-time and slow-time scales are divided by T_m, where $T_m = T_M/\sigma_M = T_N/\sigma_N$. T_m are the unified sampling periods of the energy model. Specifically, after the time-scale unification, the calculation instants of the fast-time scale are $\boldsymbol{x}_f(\zeta_0) = \boldsymbol{x}_f(nT_M)$, $\boldsymbol{x}_f(\zeta_1)$, $\boldsymbol{x}_f(\zeta_2)$, $\boldsymbol{x}_f(\zeta_3)$, $\boldsymbol{x}_f(\zeta_4)$, $\boldsymbol{x}_f((n{+}1)T_M)$, …, $\boldsymbol{x}_f(\sigma_M T_M)$, …, and the calculation instants of the slow-time scale are $z_s(\zeta_0) = z_s(nT_N)$, $z_s(\zeta_1)$, $z_s(\zeta_2)$, $\boldsymbol{x}_s(\zeta_3)$, $\boldsymbol{x}_s(\zeta_4)$, $\boldsymbol{x}_s(\zeta_5)$, $z_s((n{+}1)T_M)$, …, $z_s(\sigma_N T_N)$, …, where $\Delta\zeta_i = \zeta_i$ - $\zeta_{i\text{-}1} = T_m$ ($i = 1, 2, \ldots$). The coincident sampling instant t_0 is selected as the reference time, the full-mode operating period of the cascaded system is defined as $T_{\text{max\_com}}$. At this point, the two-time-scale system will be regarded as a whole, and the port energy calculation will be unified under the new time scale. (3) will be re-expressed as

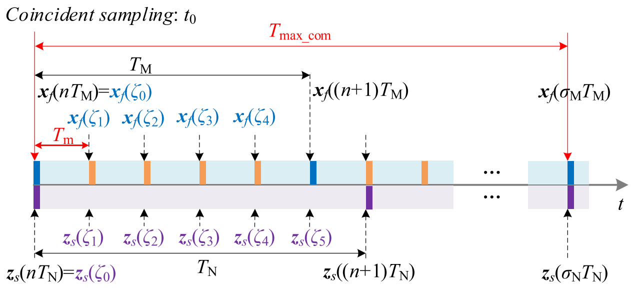

Fig. 5. The time series diagram of modeling in the unified time scale T_{m}.

$$\begin{aligned}\Delta E_{\text{bus}|T_m} &= E_{\text{bus}|T_m} - E'_{\text{bus}|T_m} \\ &= \int_t^{t+T_m} u_{C_{\text{bus}}}(\tau)\left[i_{\text{bus}}(\tau) - i'_{\text{bus}}(\tau)\right] d\tau. \end{aligned} \tag{6}$$

Theoretically, any time instant in the fast/slow-time scale can be chosen as the coincident sampling instant t_0 in Fig. 5. However, if the full-mode operating period $T_{\text{max\_com}}$ is defined such that it does not commence when the fast and slow periods are phase-coincident, it will consequently terminate at an asynchronous time instant, which complicates the synchronization of the PCCM ZVS modulation strategy [25] during the implementation of the full-mode energy control strategy. Furthermore, it will also increase the computational complexity of determining the mode rearrangement coefficients, placing the additional burden on the controller.

B. *Full-Mode Energy Model*

In [25], the four segments of the rear-end FSBB converter are represented by the unified time scale T_m, which overcome the challenge of matching the operating modes with the new time scale in the energy model computation process. As shown in Fig. 6, the mode rearrangement is required for the fast-time operation of the front-end IPT system to match the unified time scale. Considering the operating modes illustrated in Figs. 4 and 5, the port energy calculation within the period T_{M} no longer maintains half period symmetry and needs to be subdivided into five modes (i.e., modes I–V).

In mode I, assuming the system input voltage U_{in} is constant and the voltage drop on the switches is negligible, the input energy of port (a+, a-) of the cascaded system can be expressed as

$$E_{\text{in(I)}|T_m} = \int_{\zeta_0}^{\zeta_1} U_{\text{in}} \left(C_p \frac{du_{C_p}}{dt} + C_1 \frac{du_{C_1}}{dt} \right) dt$$

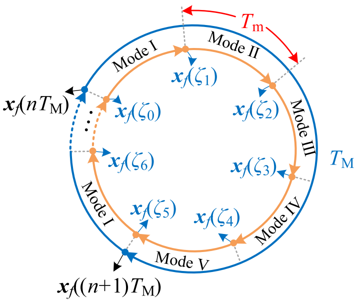

Fig. 6. Mode rearrangement for the fast-time operation of the front-end IPT system.

$$
\begin{aligned}
&= U_\mathrm{in} C_p \int_{u_{Cp}(\varsigma_0)}^{u_{Cp}(\varsigma_1)} du_{C_p} + U_\mathrm{in} C_1 \int_{u_{C_1}(\varsigma_0)}^{u_{C_1}(\varsigma_1)} du_{C_1}\\
&= U_\mathrm{in}\left[C_p\left(u_{C_p}(\varsigma_1) - u_{C_p}(\varsigma_0)\right) + C_1\left(u_{C_1}(\varsigma_1) - u_{C_1}(\varsigma_0)\right)\right]\\
&\triangleq E_{\mathrm{in}|T_m}(\varsigma_1, \varsigma_0),
\end{aligned}
\tag{7}
$$

where the capacitor voltages $u_{C\mathrm{p}}$ and u_{C1} need to be sampled at instants $t = \zeta_0 = nT_M$ and $t = \zeta_1$. Similarly, the input energy in mode II, mode IV and mode V can be calculated as $E_{\mathrm{in(II)}}(\zeta_2, \zeta_1)$, $-E_{\mathrm{in(IV)}}(\zeta_4, \zeta_3)$, and $-E_{\mathrm{in(V)}}(\zeta_5, \zeta_4)$. Mode III covers both the positive and negative half periods of the inverter waveforms, and thus can be expressed as

$$
\begin{aligned}
E_{\mathrm{in}(\perp\perp\perp)|T_m} &= \int_{\varsigma_2}^{\varsigma_2+0.5T_m} U_\mathrm{in} i_p(t)dt\\
&- \int_{\varsigma_2+0.5T_m}^{\varsigma_3} U_\mathrm{in} i_p(t)dt\\
&= E_{\mathrm{in}|T_m}(\varsigma_2 + 0.5T_m, \varsigma_2) - E_{\mathrm{in}|T_m}(\varsigma_3, \varsigma_2 + 0.5T_m).
\end{aligned}
\tag{8}
$$

where u_{Cp} and u_{C1} need to be sampled at instants $t = \zeta_2 = nT_\mathrm{M}+2T_m$ and $t = nT_M+2.5T_m$. Based on (7) and (8), the sampling frequency of the cascaded system need to be unified at $f_m = 1/(2T_m)$. It is worth noting that the division of modes should be determined based on the original operating frequency of the front-end IPT system and the unified time scale. When the number of modes is even, symmetry is observed between the positive and negative half cycles, and the selection of the modeling period T_m continues to uphold the precision of the model.

When the arbitrary instant in the duration between ζ_0 and ζ_1 is selected as t_0, implementing mode rearrangement in the front-end IPT system will necessitate at least two additional rearrangements of modes I and V to synchronize the fast and slow operating modes and match them with the unified time scale. Furthermore, the mode III no longer possesses its symmetry under this condition.

From the four-mode operation of the rear-end FSBB converter, which is shown in Fig. 4, the inductor absorbs energy from the bus capacitor in the first two modes, one can obtain the current i_bus as

$$
i_\mathrm{bus} = C_\mathrm{bus}\frac{du_{C_\mathrm{bus}}}{dt}
$$

$$
+ i'_\mathrm{bus} = C_\mathrm{bus}\frac{du_{C_\mathrm{bus}}}{dt} + i_L, t \in [nT_N, (n + D_1)T_N], \tag{9}
$$

$$
i_\mathrm{bus} = C_\mathrm{bus}\frac{du_{C_\mathrm{bus}}}{dt}, t \in [(n + D_1)T_\mathrm{N}, (n + 1)T_N]. \tag{10}
$$

Thus, the input energy of port ($b+$, b-) can be calculated as

$$
E_\mathrm{bus} = \int_t^{t+T_M} u_{C_\mathrm{bus}}(\tau)\, i_\mathrm{bus}(\tau)d\tau \tag{11}
$$

where the capacitor voltage ripple of $u_{C\mathrm{bus}}$ is considered for higher modeling accuracy. However, for the calculation of the energy of port ($b+$, b-), the operating periods of $u_{C\mathrm{bus}}$ and $i_{C\mathrm{bus}}$ are T_N and T_M, respectively. It is necessary to standardize the fast-time and slow-time variables to the unified time scale T_m. When $t\in[nT_N, (n+D_1)T_N]$, (11) can be further expressed as

$$
\begin{aligned}
E_{\mathrm{bus}|T_m} &= \int_t^{t+T_m} u_{C_\mathrm{bus}}(\tau)\, i_\mathrm{bus}(\tau)d\tau\\
&= \sum_{i=1}^{D_1\sigma_N} \frac{T_m C_\mathrm{bus}}{2}\left[u^2_{C_\mathrm{bus}}(\varsigma_i) - u^2_{C_\mathrm{bus}}(\varsigma_{i-1})\right]\\
&- \sum_{i=1}^{D_1\sigma_N} I_{L0}\left[u_{C_\mathrm{bus}}(\varsigma_i) - u_{C_\mathrm{bus}}(\varsigma_{i-1})\right]T_m\\
&+ \sum_{i=1}^{\alpha\sigma_N} \frac{1}{2L}(\sigma_N T_m)^2\left[D_1^2 + \sigma^2(D_1 - \alpha)^2\right]\\
&\left[u^2_{C_\mathrm{bus}}(\varsigma_i) - u^2_{C_\mathrm{bus}}(\varsigma_{i-1})\right].
\end{aligned}
\tag{12}
$$

When $t\in[(n+D_1)T_N, (n+1)T_N]$, one can obtain $E_\mathrm{bus}|_{Tm}$ as

$$
E_{\mathrm{bus}|T_m} = \sum_{i=D_1\sigma_N}^{\sigma_\mathrm{N}} \frac{T_m C_\mathrm{bus}}{2}\left[u^2_{C_\mathrm{bus}}(\varsigma_i) - u^2_{C_\mathrm{bus}}(\varsigma_{i-1})\right]. \tag{13}
$$

The energy of port ($c+$, c-) equal to the sum of the energy stored in the inductor and the energy consumed by the load. As illustrated in Fig. 4, the load consumes energy during the transition from the second to the third modes, and stores energy in the fourth mode. Thus, the port energy E'_bus can be expressed as

$$
\begin{aligned}
E'_\mathrm{bus} &= \int_t^{t+T_M} u_{C_\mathrm{bus}}(\tau)\, i'_\mathrm{bus}(\tau)d\tau\\
&= \int_t^{t+D_1T_M} u_L(\tau)\, i_L(\tau)d\tau.
\end{aligned}
\tag{14}
$$

For the rear-end FSBB converter under the PCCM ZVS operation, the negative valley of the inductor current is limited to -I_{L0}. Therefore, i_L can be regarded as the superposition of the component -I_{L0} and some piecewise linear smooth components. Then, (14) can be further expressed as

$$
\begin{aligned}
E'_{\mathrm{bus}|T_m} &= \int_t^{t+D_1\sigma_N T_m} -u_{C_\mathrm{bus}}(\tau)\, I_{L0}d\tau\\
&- \int_t^{t+D_1T_M} u_o(\tau)\left[i_L(\tau) + I_{L0}\right]d\tau
\end{aligned}
$$

$$
\begin{aligned}
&+\int_{t}^{t+D_1\sigma_N T_m}\left[u_{C_{\text{bus}}}(\tau)-u_{\text{o}}(\tau)\right]\left[i_L(\tau)+I_{L0}\right]d\tau\\
&=-\sum_{i=1}^{D_1\sigma_N} I_{L0}\left[u_{C_{\text{bus}}}(\varsigma_i)-u_{C_{\text{bus}}}(\varsigma_{i-1})\right]T_m\\
&+\sum_{i=1}^{\alpha\sigma_N}\frac{1}{2L}(\sigma_N T_m)^2\left[D_1^2+\sigma^2(D_1-\alpha)^2\right]\\
&\left[u_{C_{\text{bus}}}^2(\varsigma_i)-u_{C_{\text{bus}}}^2(\varsigma_{i-1})\right],
\end{aligned}
\tag{15}
$$

where D_1, α, and σ are the function of the unified time scale T_m.

Similarly, the load consumes energy in the second and third stages, thus the energy of port (d+, d-) can be expressed as

$$
\begin{aligned}
E_{o|T_m}&=\int_{\alpha}^{\alpha+D_2\sigma_N T_m} u_o(\tau)\, i_o(\tau)d\tau\\
&=\sum_{i=\alpha\sigma_N}^{(\alpha+D_2)\sigma_N}\sigma I_{L0}\left[u_{C_{\text{bus}}}(\varsigma_i)-u_{C_{\text{bus}}}(\varsigma_{i-1})\right]T_m\\
&\quad+\sum_{i=1}^{\alpha\sigma_N}\frac{1}{2L}(\sigma_N T_m)^2\left[(\sigma D_2)^2+(D_1-\alpha)^2\right]\\
&\quad\left[u_{C_{\text{bus}}}^2(\varsigma_i)-u_{C_{\text{bus}}}^2(\varsigma_{i-1})\right].
\end{aligned}
\tag{16}
$$

From (15) and (16), it can be observed that the port energy $E'_{\text{bus}|Tm}$ and $E_{o|Tm}$ are the functions of D_1, D_2, and α and taking the unified time scale T_m as the calculation step size ensures the tracking of the variations in the average inductor current $\langle i_L\rangle$ over slow-time period T_N.

According to the port energy $E_{\text{o}|Tm}$, one can obtain the output current of the load battery i_{o} during the slow-time period T_{N}, which is

$$
\text{i}_{o|T_m}(\sigma,D_1,D_2,\alpha,u_{C_{\text{bus}}})=E_{o|T_m}/\left[\sigma\sigma_{\text{N}}u_{C_{\text{bus}}}(\varsigma_i)\,T_m\right].
\tag{17}
$$

The output power of the cascaded IPT-FSBB system can be expressed as

$$
P_{o|T_m}(\sigma,D_1,D_2,\alpha,u_{C_{\text{bus}}})=E_{o|T_m}/(\sigma_N T_m).
\tag{18}
$$

It can be observed from (16) and (17) that the calculation of the output port energy $E_{o|Tm}$ and load current $i_{o|Tm}$ of the two-time-scale cascaded system is independent of the equivalent load resistance and load voltage, which means that when implementing the energy control strategy for the system, there is no need to sample the load voltage and current. Moreover, the calculations of $E_{\text{bus}|Tm}$, $E'_{\text{bus}|Tm}$, and $E_{o|Tm}$ all depend on the bus capacitor voltage $u_{C\text{bus}}$.

C. Correction of the Unified Time Scale

In Fig. 5, the fast time scale $f_M = 1/T_M$ and the slow time scale $f_N = 1/T_N$ are discretized into five and six intervals, by the new time scale T_m, respectively. Nevertheless, due to the variability in operating frequencies of different two-time-scale systems, the selection of a unified time scale is not uniquely determined. Choosing a very small unified time scale can theoretically enhance the accuracy of the energy model when analyzing the two-time-scale systems, while significantly increases the computational burden on the processor. Here, a simple method is proposed to correct the unified time scale

$$
\hat{T}_m=[T_m]+K_0 t_d
\tag{19}
$$

where t_d is the dead time for achieving ZVS of the MOSFETs, which is given as $t_d = 300$ ns in this article. $[T_m]$ represents selection of the closest feasible value that satisfies $f_m = 1/T_m$, where f_m needs to be an integer multiple of 1 kHz. $K_0 = 0, \pm1, \pm2, \ldots$, which is used to compensate for numerical bias in the time-scale unification. Thus, the range of unified time scale is [t_d, 1/f_M], where f_M is the fast time scale of the multiple-time-scale systems.

In the systems where the fast and slow time scales are nearly identical, employing a single-time-scale energy model will offer a trade-off between the computational complexity and model accuracy. More specifically, when $f_M = f_N$, to ensure that the energy model can still capture the dynamic response of transitions between system operating states, the unified time scale can be set to $T_m = 0.1/f_M = 0.1/f_N$, and the mode arrangement in the full-mode period is also required.

TABLE I
PARAMETERS OF THE TWO-TIME-SCALE IPT-FSBB SYSTEM

Parameters	Values	Parameters	Values
L_1	75.7 μH	L_2	77.5 μH
L_{p}	41.5 μH	L_{s}	41.5 μH
C_1	102.5 nF	C_2	97.4 nF
C_{p}	83.7 nF	C_{s}	84.5 nF
L_{f}	55 μH	C_{bus}	5 μF
ε	0.125-3.375	f_{N}	40 kHz

D. Verification in Simulations

To verify the correctness of the proposed two-time-scale energy model, a time-domain simulation with the system parameters given in Table I, where the equivalent series resistances of the inductors and capacitors are neglected, is conducted for comparison. It is worth noting that the single-time-scale energy model cannot simultaneously calculate variables in two different time scales. Therefore, before solving the single-time-scale energy model, it is necessary to decouple the cascaded system, which means that the bus voltage $u_{C\text{bus}}$ is constant and that there is no energy loss between port (b+, b-) and port (d+, d-).

Fig. 7(a) presents the comparison of the output current i_o obtained by the time-domain simulations and the energy model, where a step change of $\Delta\alpha = 2\hat{T}_m$ is added to the phase-shift α_n at t = 2 ms. As illustrated in Fig. 7(a), the two-time-scale energy model, by applying time-scale transformation and mode rearrangement, is capable of precisely capturing the dynamic response characteristics of i_o. Compared to the discrete-time mapping model in [25], the two-time-scale energy model significantly reduces computational burden, thereby facilitating more effective control design of the cascaded system. As discussed in Section II-C, the single-time-scale energy model fails to consider the variations of the inductor current i_L within the slow-time period T_N. As a result, when the operating state of

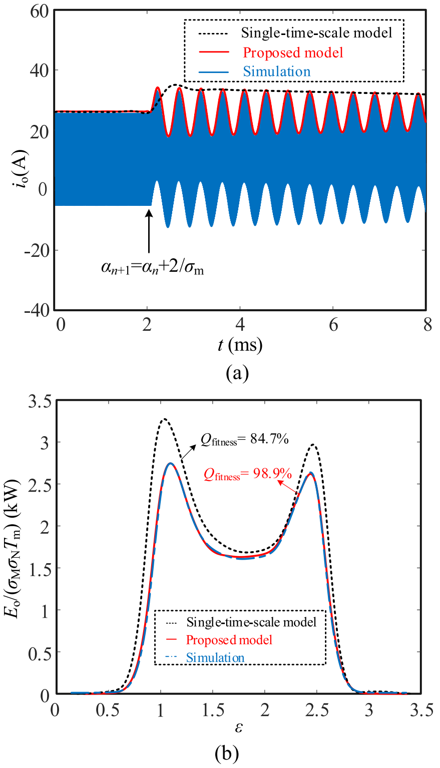

(a)

(b)

Fig. 7. Responses of the time-domain simulations, the single-time-scale energy model, and the proposed two-time-scale energy model. (a) Output current i_o with a step increment of the phase-shift α_n of $2\hat{T}_m$ when $D_1 = 0.4$, $D_2 = 0.6$, $f_M = 85$ kHz, $f_N = 40$ kHz, and $U_{\text{in}} = U_o = 300$ V. (b) The average value of the port energy $E_{o|Tm}$ in the full-mode operating period $T_{\text{max\_com}}$ with ε varying from 0.125 to 3.375 when $D_1 = 0.4$, $D_2 = 0.6$, $\alpha = 0.2$, $f_N = 40$ kHz, and $U_{\text{in}} = U_o = 300$ V.

the rear-end FSBB converter changes, it only reflects the general trend of current changes and has poor performance in tracking the system's dynamic response.

Fig. 7(b) illustrates the comparison of the average output energy of port (d+, d-) over full-mode period $T_{\text{max\_com}} = \sigma_M\sigma_N T_m$ as the ratio ε of the two time scales varies from 0.125 to 0.375. Q_{fitness} is utilized as a metric for assessing the accuracy of the model's results and is defined as

$$Q_{\text{fitness}} = \left(1 - \frac{\| A - \hat{A}\|_2}{\| \hat{A} - \text{mean}\left\{\hat{A}\right\} \|_2}\right) \times 100\% \tag{20}$$

where A is the results derived from the single-time-scale and two-time-scale energy models, $\hat{A}$ is the system output in simulations.

In Fig. 7(b), the selection of the unified time scale T_m is not constant but varies with ε, which demonstrates that the two-time-scale energy model exhibits robust accuracy over a wide range of variations in T_m, maintaining an accuracy Q_{fitness} above 98.9%. Conversely, the single-time-scale energy model aligns well with the simulation results only when there is a substantial difference between the two time scales.

The presented results in Fig. 7 illustrates that the predicted response of the proposed energy model agrees well with both the dynamic and steady-state responses obtained from simulations. Consequently, it addresses the limitation of inadequate dynamic response tracking existing in the single-time-scale energy model. Additionally, it alleviates the computational burden associated with applying such models to cascaded systems.

IV. FULL-MODE ENERGY CONTROL

A. *Small-Signal Model*

The port energy of the cascaded system under conditions of incomplete decoupling can be obtained from the unified two-time-scale energy model. Furthermore, when the fast-time-scale IPT system operates at resonant frequency, the output of the *LCC-LCC* compensation network features constant-current output characteristic [26], and $i_{\text{bus}}(t) = \pi I_{\text{bus}}|\sin(\omega_M t)|/2$, where I_{bus} is the average value of i_{bus} in the fast-time period T_M. In the full-mode energy control, the power interaction between the two stages cannot be ignored and the output power can be adjusted with the two duty cycles of the rear-end FSBB converter. Therefore, the two-time-scale IPT-FSBB system can be equivalent to the topology depicted in Fig. 9 with preserving the energy coupling port (c+, c-) and maintaining the unchanged energy transfer characteristics of the cascaded system.

As shown in Fig. 5, when the sampling instants of the fast-time and slow-time scales coincide, the control variables are calculated simultaneously, thus, the composite control is conducted in the full-mode period $T_{\text{max\_com}} = \sigma_M\sigma_N T_m$. The relationship between the input and output currents can be obtained as

$$I_{o|T_{\text{max\_com}}} = \mathrm{D}_1 I_{\text{bus}|T_{\text{max\_com}}} \tag{21}$$

where $I_{o|\,T\text{max\_com}}$ are the average values of i_o and i_{bus} in the full-mode operating period $T_{\text{max\_com}}$, respectively.

In the steady state, the state-space average model of the system shown in Fig. 9 can be expressed as

$$\begin{cases} C_{\text{bus}}\dfrac{\partial\langle u_{C\text{bus}}(t)\rangle_{T\text{max\_com}}}{\partial t} = \langle i_{\text{bus}}\left(t\right)\rangle_{T_{\text{max\_com}}} - D_1\langle i_L\left(t\right)\rangle_{T_{\text{max\_com}}} \\ L\dfrac{\partial\langle i_L(t)\rangle_{T\text{max\_com}}}{\partial t} = D_1\langle u_{C\text{bus}}\left(t\right)\rangle_{T_{\text{max\_com}}} - D_2\langle u_o\left(t\right)\rangle_{T_{\text{max\_com}}} \\ C_o\dfrac{\partial\langle u_o(t)\rangle_{T\text{max\_com}}}{\partial t} = D_2\langle i_L\left(t\right)\rangle_{T_{\text{max\_com}}} - \langle u_{\text{o}}\left(t\right)\rangle_{T_{\text{max\_com}}}/R_{\text{o}} \end{cases}. \tag{22}$$

By adding the small-signal perturbations $\hat{i}_{\text{bus}}$, $\hat{u}_{C_{\text{bus}}}$, $\hat{i}_L$, $\hat{u}_o$, $\hat{d}_1$, $\hat{d}_2$ to (22) and via Laplace transform, the input-to-output and control-to-output transfer function can be obtained as

$$G_{I_{\text{bus}}-u_{C\text{bus}}}\left(s\right) = \hat{u}_{C_{\text{bus}}}\left(s\right)/\hat{i}_{\text{bus}}\left(s\right)$$
$$= \frac{C_oLR_os^2 + Ls + D_2^2}{C_oC_{\text{bus}}LR_os^3 + C_{\text{bus}}Ls^2 + \left(D_1^2C_o + D_2^2C_{\text{bus}}\right)R_os + D_1^2}, \tag{23}$$

$$G_{d_1-u_{C\text{bus}}}\left(s\right) = \hat{u}_{C\text{bus}}\left(s\right)/\hat{d}_1\left(s\right) =$$
$$\frac{-I_{\text{bus}}\left[D_1^2C_oLR_os^2 + \left(D_2^2R_o^2C_o + D_1^2L\right)s + D_2^2R_o\left(D_1^2 + 1\right)\right]}{D_1\left[C_oC_{\text{bus}}LR_os^3 + C_{\text{bus}}Ls^2 + \left(D_1^2C_o + D_2^2C_{\text{bus}}\right)R_os + D_1^2\right]} \tag{24}$$

$$G_{d_2-u_{C\text{bus}}}\left(s\right) = \hat{u}_{C\text{bus}}\left(s\right)/\hat{d}_2\left(s\right)$$
$$= \frac{D_2R_oI_{\text{bus}}\left(C_oR_os + D_1^2 + 1\right)}{C_oC_{\text{bus}}LR_os^3 + C_{\text{bus}}Ls^2 + \left(D_1^2C_o + C_{\text{bus}}D_2^2\right)R_os + D_1^2}. \tag{25}$$

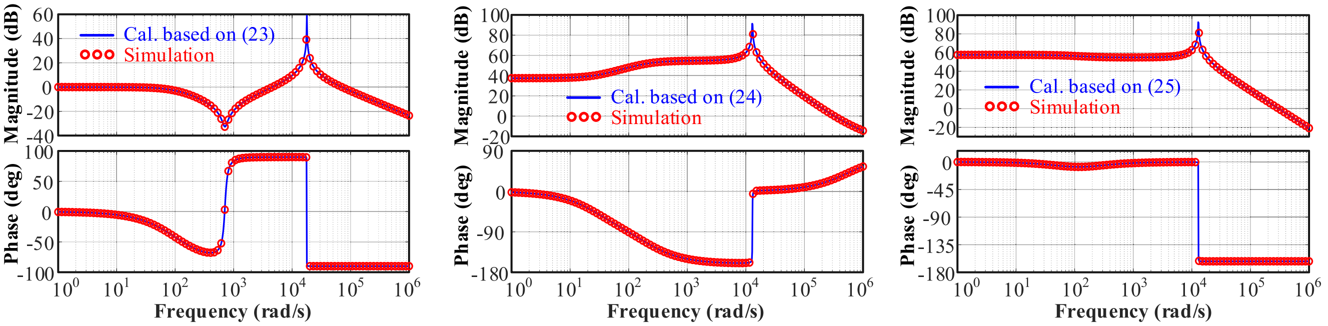

(a) (b) (c)

Fig. 8. Verification of the small-signal model. (a) $G_{I_{\text{bus}}-u_{C_{\text{bus}}}}$. (b) $G_{d_1-u_{C_{\text{bus}}}}$. (c) $G_{d_2-u_{C_{\text{bus}}}}$.

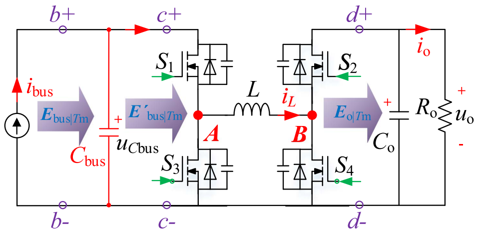

Fig. 9. Equivalent circuit of the slow-time-scale FSBB converter.

Different from the single-time-scale models, the average model in (22) and the small-signal model are unified as the full-mode period $T_{\max\_\text{com}} = 1/f_{\max\_\text{com}}$, which means that Laplace operator $s = j\omega = j2\pi f_{\max\_\text{com}}$, overcoming the difficulty of solving for variables existing in different time scales within one same equation.

Fig. 8verifies the small-signal model of the cascaded system, comparing the transfer functions predicted by (23)–(25) with those obtained from the frequency response measurements performed in the simulation. In particular, the simulation parameters are given in Table I and $D_1 = 0.5$, $D_2 = 0.5$, $I_{\text{bus}} = 4.85$ A, $C_{\text{o}} = 300\ \mu$F, $C_{\text{bus}} = 5\ \mu$F, $L = 55\ \mu$H, $R_o = 30\ \Omega$. In simulations, a sine wave at different frequencies serves as the perturbation of the duty cycles D_1 and D_2. The results presented in Fig. 8 demonstrate a good agreement between the theoretical model and simulation results across the full frequency range, except for the minor deviations near the resonant point, which validates the accuracy of the theoretical analysis.

B. Proposed Energy Control Strategy

The close-loop structure of the proposed composite control strategy is shown in Fig. 10, where $I_{L\_\text{ZVS}} = 2C_{\text{oss}}U_{C\text{bus}}/t_{\text{d}} + U_{C\text{bus}}t_d/L$, K_{C1} and K_{Cp} serve as the proportionality coefficients for determining the input energy in (7) and (8). The synchronous rectification is employed in the fast-time-scale IPT system. The symmetric-on-time single-update digital pulsewidth modulation algorithm is adopted to generate the driving signals $v_{gQ11}\sim v_{gQ14}$ and $v_{gS1}\sim v_{gS4}$ of the primary-side inverter and the rear-end FSBB converter, respectively.

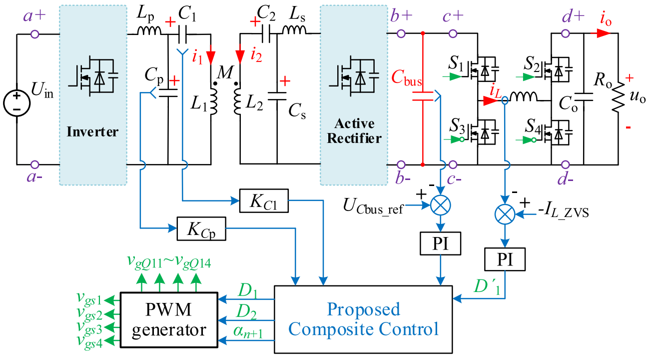

Fig. 10. Two-time-scale cascaded FSBB-IPT system with the proposed composite energy control.

In contrast to output current and voltage control, the energy control strategy studied in this article selects the port energy of the cascaded system as the control target. The two-time-scale energy model derived in Section III shows that the calculation of the port energy $E_{\text{in}|Tm}$, $E_{\text{bus}|Tm}$, $E'_{\text{bus}|Tm}$, and $E_{o|Tm}$ are independent of the load current i_{o}. Furthermore, as can be seen from (17), the changes in i_{o} can be accurately tracked by the output port energy $E_{o|Tm}$. Therefore, it is not necessary to sample the load current. In fact, the energy consumed by the load is determined by the energy of the port ($c+$, c-) and the four-mode operation of the rear-end FSBB converter. In consideration of the energy interaction between the bus capacitor and the port ($b+$, b-), the optimal control target of the two-time-scale cascaded system is $E_{\text{bus}|Tm}$.

In the single-time-scale energy control method, the two stages of the cascaded system are considered decoupled, and the voltage variation of the dc bus and the energy storage elements is zero. However, under the nonfully decoupling conditions, there is energy interaction between the bus capacitor and the inductor. Therefore, the inductor current i_L need to be sampled for ZVS and minimum rms current operation of the rear-end FSBB converter. In the composite energy control strategy studied in this article, the inductor current is controlled by adjusting the duty cycles D_1, D_2, and the phase-shift α, which are also relevant to the energy of ports ($c+$, c-) and ($d+$, d-). Specifically, the input

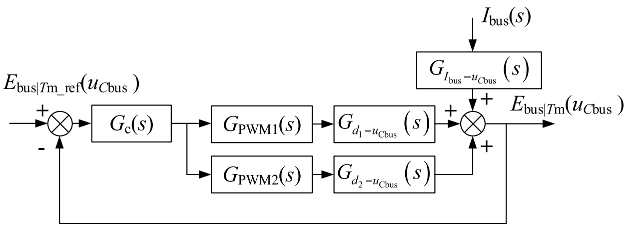

Fig. 11. Block diagram of the full-mode energy control.

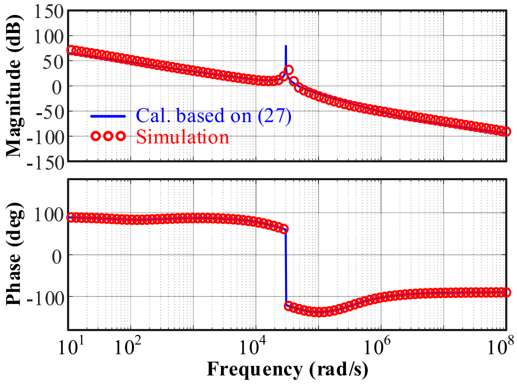

Fig. 12. Verification of the small-signal model of $G_{\mathrm{op}\_E_{\mathrm{bus}}}(s)$ when $k_p/k_m = -0.252$ and $k_i/k_m = -9470.6$.

energy $E_{\mathrm{in}|Tm}$ is calculated based on the capacitor voltages u_{C1} and u_{Cp}, the output energy of the port ($c+$, c-) can be obtained by the bus voltage $u_{C\mathrm{bus}}$ based on (12) and (13).

The block diagram of the proposed energy control strategy conducted in the full-mode period $T_{\max\_\mathrm{com}}$ is shown in Fig. 11, which is implemented in the microcontroller TMS320F28335. The port energy cannot be directly measured through hardware design, as analyzed in Section III-B, the voltage of the bus capacitor $u_{C\mathrm{bus}}$ can be chosen as the sampling variable for the energy control strategy. In Fig. 11, the control variable $u_{C\mathrm{bus}}$ is determined by $(\sigma_{\mathrm{M}}\sigma_{\mathrm{N}}E_{\mathrm{bus}|Tm})/(I_{\mathrm{bus}|T\max\_\mathrm{com}})$, and $G_c(s)$ is the transfer function of the PI controller, which can be expressed as

$$G_c(s) = k_p + \frac{k_i}{s} \tag{26}$$

where k_p and k_i are the proportional coefficient and integral coefficient, respectively. $G_{\mathrm{PWM}i}(s) = 1/k_{mi}$ ($i = 1$ and 2) serve as proportional gains utilized in the generation of the duty cycles D_1 and D_2, where k_{mi} is the amplitude of the carrier.

C. Closed-Loop Characteristics

The open-loop transfer function of the energy control strategy shown in Fig. 11 is

$$G_{\mathrm{op}\_E_{\mathrm{bus}}}(s) = G_c(s)\left[G_{\mathrm{PWM1}}(s)\,G_{d_1-u_{C\mathrm{bus}}}(s) + G_{\mathrm{PWM2}}(s)\,G_{d_2-u_{C\mathrm{bus}}}(s)\right]. \tag{27}$$

Then, one can obtain the closed-loop transfer function for the full-mode control as

$$G_{\mathrm{cl}\_E_{\mathrm{bus}}}(s) = \frac{G_{\mathrm{op}\_E_{\mathrm{bus}}}(s)}{1 + G_{\mathrm{op}\_E_{\mathrm{bus}}}(s)}. \tag{28}$$

The detailed expression of $G_{\mathrm{cl}\_E_{\mathrm{bus}}}(s)$ is given at the bottom of this page.

Different from the buck, buck-boost, and boost converters, the FSBB converter has two duty-cycles (i.e., D_1 and D_2) that need to be controlled, and $G_{d_1\_u_{C\mathrm{bus}}}$ and $G_{d_2\_u_{C\mathrm{bus}}}$ may have right-half-plane zeros. Therefore, it is necessary to investigate the impact of the key parameters on the stability of the energy control loop. Considering the characteristic of incomplete decoupling in the two-time-scale systems, the analysis is mainly focused on C_{bus}, k_p, k_i, and R_o.

Given the parameters as: $D_1 = 0.5$; $D_2 = 0.4$; $I_{\mathrm{bus}} = 4.85$ A; $C_{\mathrm{o}} = 300\ \mu$F, $C_{\mathrm{bus}} = 5\ \mu$F; $L = 55\ \mu$H; and $R_o = 30\ \Omega$. The small-signal model obtained from (27) is verified in Fig. 12, which exhibits good agreement between the theoretical analysis and the simulation results. Fig. 13(a) and (b) shows the Bode plots and pole-zero maps of $G_{\mathrm{op}\_E_{\mathrm{bus}}}(s)$ and $G_{\mathrm{cl}\_E_{\mathrm{bus}}}(s)$ as the bus capacitor C_{bus} varies from 5 to 35 μF. It can be seen from Fig. 13(a) that as the C_{bus} increases, the crossover frequency of $G_{\mathrm{op}\_E_{\mathrm{bus}}}(s)$ decreases, while the phase margin increases. The resonant peak magnitude of the Bode plot decreases accordingly, implying that a higher bus capacitance in the two-time-scale system contributes to improving stability margin. In Fig. 13(b), the closed-loop transfer function possesses three zeros, all of which are situated in the left-half plane, and they are not affected by C_{bus}. A pair of conjugate poles moves towards both the real and imaginary axes as C_{bus} increases, and the other poles are located on the real axis and approaches the origin.

Fig. 13(c) and (d) shows the Bode plots and pole-zero maps of $G_{\mathrm{op}\_E_{\mathrm{bus}}}(s)$ and $G_{\mathrm{cl}\_E_{\mathrm{bus}}}(s)$ as k_p/k_m varies from -0.30259 to -0.00259. The low-frequency gain, resonant frequency, and resonant peak magnitude remain unchanged with variations in k_p, indicating that the low-frequency characteristic is unaffected by k_p, whereas the phase margin increases as k_p increases. A pair of conjugate poles move away from their initial positions closer to the imaginary axis, progressively approaching the real axis. In contrast, the additional two poles exhibit no change in position with variations in k_p, indicating their independence from k_p.

Fig. 13(e), (f) show the Bode plots and pole-zero maps of $G_{\mathrm{op}\_E_{\mathrm{bus}}}(s)$ and $G_{\mathrm{cl}\_E_{\mathrm{bus}}}(s)$ as k_i/k_m varies from -14710.6

$$G_{\mathrm{cl}\_E_{\mathrm{bus}}}(s) = \frac{-I_{\mathrm{bus}}(k_p s + k_i)\,X(s)}{D_1 k_m\left[C_o C_{\mathrm{bus}} L R_o s^4 + C_{\mathrm{bus}} L s^3 + \left(D_1^2 C_o + D_2^2 C_{\mathrm{bus}}\right) R_o s^2 + D_1^2 s\right] - I_{\mathrm{bus}}(k_p s + k_i)\,X(s)}.$$

$$X(s) = D_1^2 C_o L R_o s^2 + \left(D_2^2 R_o C_o + D_1^2 L - D_1 D_2 R_o^2 C_o\right) s + R_o\left(D_1^2 + 1\right)\left(D_2^2 - D_1 D_2\right)$$

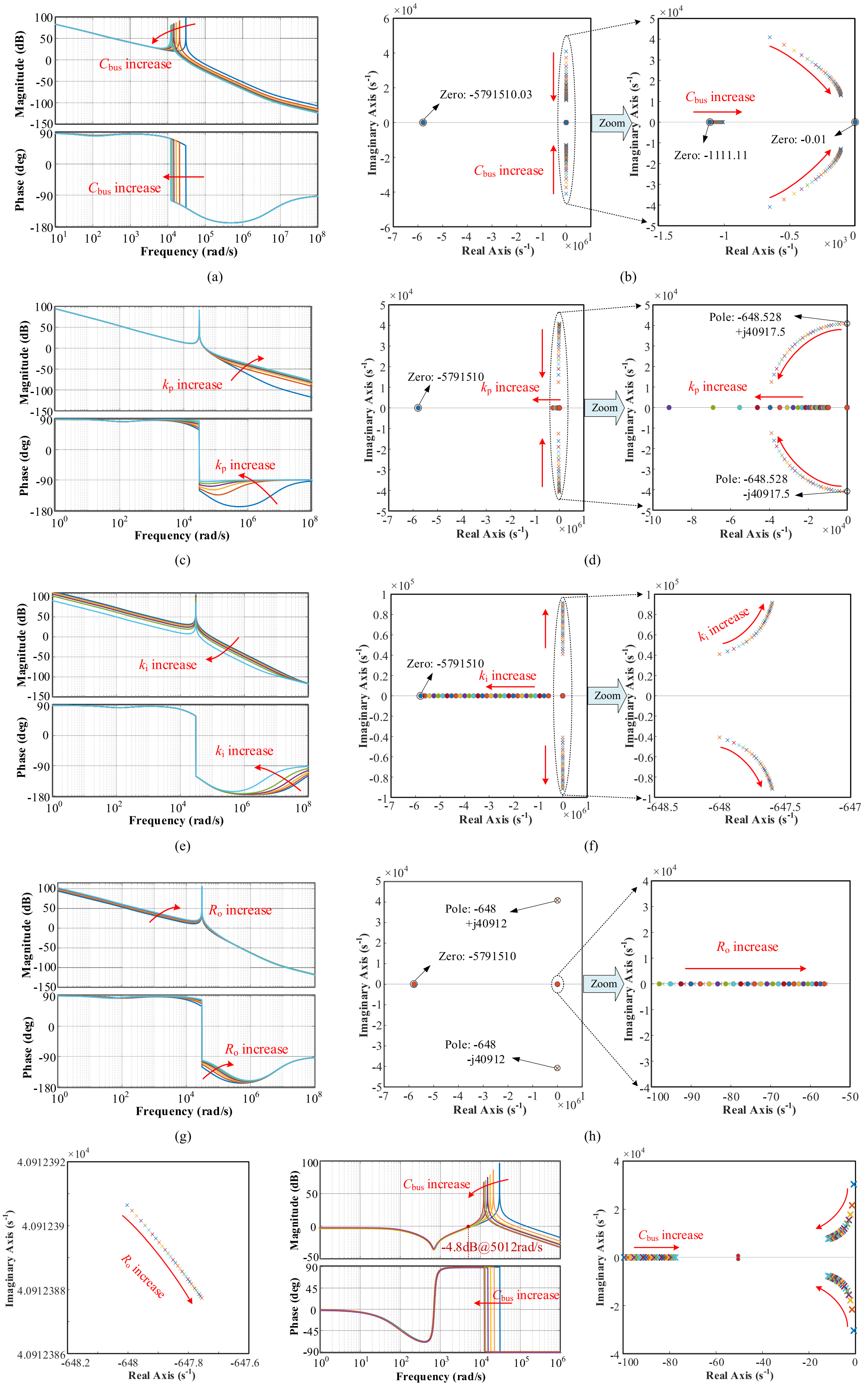

(a) (b) (c) (d) (e) (f) (g) (h) (i) (j) (k)

Fig. 13. Bode plots and Pole-zero map of the of the full-mode control loop gains. (a) Bode plot of $G_{\text{op}\_E_{\text{bus}}}$ $G_{\text{op}\_E_{\text{bus}}}(s)$ as C_{bus} increase. (b) Poles and zeros of $G_{\text{cl}\_E_{\text{bus}}}(s)$ as C_{bus} increase. (c) Bode plot of $G_{\text{op}\_E_{\text{bus}}}$ $G_{\text{op}\_E_{\text{bus}}}(s)$ as k_{p} increase. (d) Poles and zeros of $G_{\text{cl}\_E_{\text{bus}}}(s)$ as k_{p} increase. (e) Bode plot of$G_{\text{op}_E_{\text{bus}}}$ $G_{\text{op}\_E_{\text{bus}}}(s)$ as k_i increase. (f) Poles and zeros of $G_{\text{cl}\_E_{\text{bus}}}(s)$ as k_i increase. (g) Poles and zeros of $G_{\text{cl}\_E_{\text{bus}}}(s)$ as R_o increase. (h) Bode plot of$G_{\text{op}_E_{\text{bus}}}$ $G_{\text{op}\_E_{\text{bus}}}(s)$

to -4710.6. In Fig. 13(e), the low-frequency gain decreases as k_i/k_m increases, while the control bandwidth narrows. In Fig. 13(f), a pair of conjugate poles move away from the real axis and towards the imaginary axis, but their range of movement is limited. One of the zeros progressively migrates away from the origin, exhibiting a considerable range of movement.

Fig. 13(g), (h), and (i) shows the Bode plots and pole-zero maps of $G_{\text{op}\_E_{\text{bus}}}(s)$ and $G_{\text{cl}\_E_{\text{bus}}}(s)$ as R_o varies from 30 to 90 Ω. In Fig. 13(g), when the frequency is lower than the crossover frequency, the low-frequency gain increases with the increase of R_o, however, in the high-frequency gain of $G_{\text{op}\_E_{\text{bus}}}(s)$ remains almost unchanged. Meanwhile, the phase margin increases with the increase of R_o. Similarly, in Fig. 13(h) and (i), the distribution of zeros and poles remains largely invariant to changes in the load, except for one zero and one pole located on the real axis, which are observed to move progressively closer to the origin.

In Fig. 13(b), (d), (f), and (h), the positions of the two zeros closest to and farthest from the origin remain constant, indicating that they are minimally affected by changes in C_{bus}, k_p, k_i, and R_o.

Fig. 13(j) and (k) presents the Bode plots and pole-zero maps of $G_{I_{\text{bus}}\_u_{C\text{bus}}}(s)$ as C_{bus} varies from 5 to 35 μF. In Fig. 13(j), although the resonant frequency and resonant peak shift to the left with changes in C_{bus}, the amplitude margin and phase margin remain unchanged. Moreover, it can be seen from Fig. 13(j) that the low-frequency gain of $G_{\text{op}\_E_{\text{bus}}}(s)$ remains constant and below -4.8 dB, which means that it can effectively suppress low-frequency input below 5012 rad/s. In Fig. 13(k), the distribution of zeros is not affected by C_{bus}, while a pair of conjugate poles move closer to the real axis as C_{bus} increases, and another pole located on the real axis gradually approaches the origin.

According to the aforementioned analysis, the composite energy control strategy possesses excellent low-frequency input suppression characteristic. Besides, despite the presence of multiple zeros and poles in the control loop, their locations in the left half-plane of the complex plane serve as a clear indication of the system's stability. Furthermore, it is evident that C_{bus}, k_p and k_i have a substantial influence on the energy control loop, while the load R_o exhibits little effect on the control loop's performance. Consequently, it further substantiates the energy control strategy can eliminate the need for sampling load voltage and current, thereby reducing the cost and complexity of hardware design, as well as reducing the computational burden on the controller.

D. *Effect of the Bus Capacitor*

In the two-time-scale cascaded IPT-FSBB systems, the bus capacitor C_{bus} facilitates power interaction between the two stages. The energy of port (c+, c-) is chosen as the control objective for full-mode energy control strategy. To further analyze the impact of the bus capacitor C_{bus} on the system's frequency-response characteristics, the small-signal model derived from the full-mode energy control strategy, impedance-based small-signal model [29], and multifrequency-domain small-signal model [30] are compared.

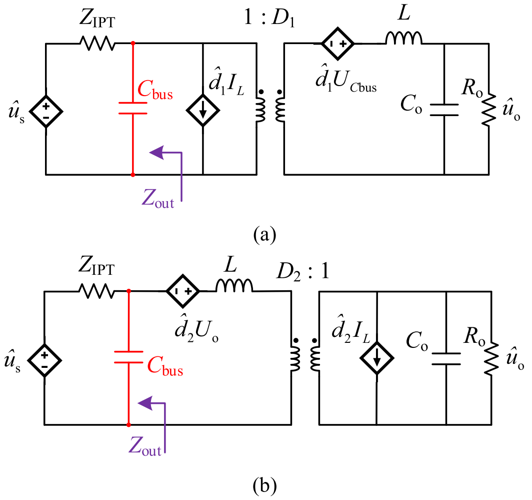

(a)

(b)

Fig. 14. Impedance-based small-signal model of the cascaded IPT-FSBB system. (a) Buck mode. (b) Boost mode.

1) Impedance-based small-signal model: Fig. 14(a) and (b) shows the impedance-based small-signal model of the cascaded IPT-FSBB system in buck and boost mode, respectively. Z_{out} is the output impedance, which includes the bus capacitor C_{bus}. In buck mode, the control-to-output gain of the system can be obtained as

$$G_{d_1-u_o}(s) = \frac{\left[1 - D_1^2 Z_{\text{out}}(s)/R_o\right] U_{C\text{bus}}}{(1+R_oC_os)\left[Ls + D_1^2 Z_{\text{out}}(s)\right]/R_o + 1}. \tag{29}$$

In boost mode, the control-to-output gain is

$$G_{d_2-u_o}(s) = \frac{-\left[Z_{\text{out}}(s) + sL\right] U_{C\text{bus}}}{(1+R_oC_os)\left[Ls + Z_{\text{out}}(s)\right] + D_1^2 R_o}. \tag{30}$$

Under the resonant condition, the control-to-output gains $G_{d_1\_u_o}$ and $G_{d_2\_u_o}$ at different C_{bus} are presented in Fig. 15 with the output impedance Z_{out} in [31].

In buck mode, it can be seen from Fig. 15(a) that in the impedance-based small-signal model, the influence of the bus capacitor C_{bus} is confined to the magnitude and phase response of the transfer function $G_{d_1\_u_o}$ at medium frequencies, with minimal impact observed on the low-frequency and high-frequency regions. However, in boost mode shown in Fig. 15(b), the bus capacitor primarily influences the magnitude response of $G_{d_2\_u_o}$ in the medium-to-high frequency range. The crossover frequency decreases as the bus capacitance C_{bus} increases. Furthermore, when C_{bus} exceeds 12.5μF, the phase response undergoes substantial alterations.

The output impedance Z_{out} of the LCC-LCC IPT system is a fifth-order expression [31]. Consequently, compared to the third-order small-signal model (24) and (25) of full-mode energy control, the impedance-based small-signal model of the two-time-scale cascaded IPT-FSBB system exhibits a higher order and imposes a greater computational burden. Furthermore, the phase-frequency characteristics of the output-to-control transfer function $G_{d_1\_u_o}$ and $G_{d_2\_u_o}$ are significantly influenced by

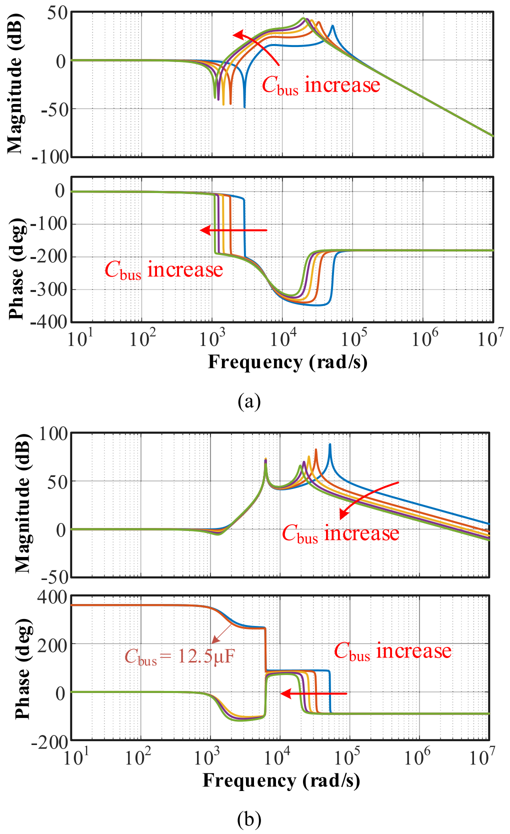

Fig. 15. Bode plots of the impedance-based small-signal model in [29] when C_{bus} varies from 5μF to 35μF. (a) $G_{d_1\_u_o}$, $D_1 = 0.4$, and $D_2 = 0.5$. (b) $G_{d_2\_u_o}$, $D_1 = 0.5$, and $D_2 = 0.4$.

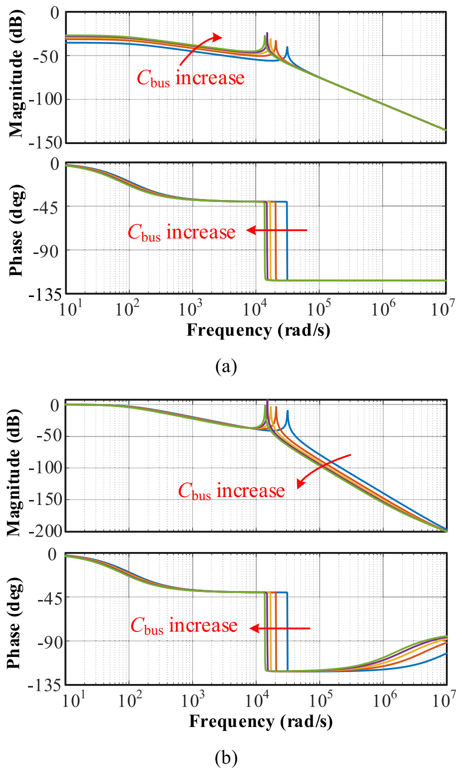

Fig. 16. Bode plots of the impedance-based small-signal model in [30] when C_{bus} varies from 5 to 35 μF. (a) $G_{d_1\_u_o}$, $D_1 = 0.4$, and $D_2 = 0.5$. (b) $G_{d_2\_u_o}$, $D_1 = 0.5$, and $D_2 = 0.4$.

the bus capacitance C_{bus} within the low-to-medium frequency range. In contrast, under the full-mode energy control strategy illustrated in Fig. 13(a), the frequency characteristics of the open-loop gain $G_{\text{op}\_E_{\text{bus}}}(s)$ maintain a relatively flat behavior, which further demonstrates the robustness of the full-mode energy control strategy.

2) Multifrequency-domain small-signal model: The time-domain variables $u_{C\text{bus}}$, i_{bus}, i'_{bus}, i_L, u_o of (22) are represented as $\boldsymbol{U}_{C\text{bus}}$, $\boldsymbol{I}_{\text{bus}}$, $\boldsymbol{I'}_{\text{bus}}$, $\boldsymbol{I}_L$, $\boldsymbol{U}_o$ in the multifrequency-domain model [30]. After the Fourier coefficients decomposition and multifrequency-domain convolution of the multiplication terms, the state-space average model of (22) can be rewritten as

$$\begin{cases} C_{\text{bus}}\left(\frac{\partial \boldsymbol{U}_{C_{\text{bus}}}}{\partial t}+\boldsymbol{\Omega}\boldsymbol{U}_{C_{\text{bus}}}\right)=\boldsymbol{I}_{\text{bus}}-\boldsymbol{S}_{\text{sw1}}\boldsymbol{I}_L \\ L\left(\frac{\partial \boldsymbol{I}_L}{\partial t}+\boldsymbol{\Omega}\boldsymbol{I}_L\right)=\boldsymbol{S}_{\text{sw1}}\boldsymbol{U}_{C_{\text{bus}}}-\boldsymbol{S}_{sw2}\boldsymbol{U}_{C_{\text{bus}}} \\ C_o\left(\frac{\partial \boldsymbol{U}_o}{\partial t}+\boldsymbol{\Omega}\boldsymbol{U}_o\right)=\boldsymbol{S}_{\text{sw2}}\boldsymbol{I}_L-\boldsymbol{U}_o/R_o \end{cases} \tag{31}$$

where $\boldsymbol{S}_{\text{sw}\,i} = 0$ or 1 when S_1/S_2 are on/off. The diagonal matrix $\boldsymbol{\Omega} = \text{Diag}[j4\sigma_M\pi f_m, \ldots, j2\pi f_m, 0, -j2\pi f_m, \ldots, \text{-}j4\sigma_M\pi f_m]$. By linearizing the state-space model (31), the results of the small-signal response of the output voltage $\hat{u}_{\text{o}}$ to the duty cycles $\hat{d}_1$ and $\hat{d}_2$ with different C_{bus} are presented in Fig. 16.

As shown in Fig. 16(a), in the multifrequency small-signal model, the increasing C_{bus} elevates the magnitude curve of $G_{d_1\_u_o}$ in the low-to-medium frequency band, while exerting no influence on its high-frequency response. Conversely, for $G_{d_2\_u_o}$, the low-frequency magnitude curve remains unaffected by C_{bus}, whereas its magnitude in the medium-to-high frequency band decreases as C_{bus} increases.

The fundamental frequency f_m enables the derivation of third-order multi-frequency-domain small-signal model, which demonstrates relatively mild susceptibility to the C_{bus} changes, akin to the frequency behavior characteristic of the $G_{\text{op}\_E_{\text{bus}}}(s)$ of the full-mode energy control strategy. Nevertheless, the necessity for Fourier operations augments the complexity of the model derivations.

E. PI Controller Design

To further analyze the impact of PI parameters on the stability and dynamic response of two-time-scale systems under full-mode energy control, the design of parameters k_p, k_i is conducted using Bode plots of the open-loop transfer function $G_{\text{op}\_E_{\text{bus}}}(s)$. For the PI parameter design, the following two criteria need to be satisfied: the phase margin should exceed 45° and the crossover frequency should be as large as possible to enhance the system's dynamic response speed.

It can be seen from Fig. 13 that the crossover frequency of $G_{\text{op}\_E_{\text{bus}}}(s)$ is predominantly determined by the integral coefficient k_i, with the proportional coefficient k_p exhibiting minimal influence. Moreover, the gain margin consistently satisfies stability requirement. Conversely, the phase margin is primarily determined by k_p, while k_i contributes negligibly to it. Therefore,

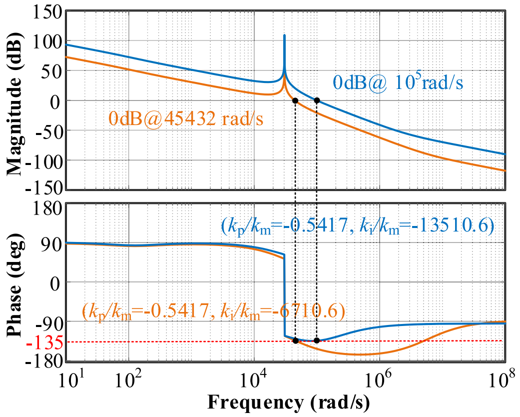

Fig. 17. Bode plots of $G_{\text{op\_}E_{\text{bus}}}(s)$ for PI parameter design when $D_1 = D_2 = 0.5$, $I_{\text{bus}} = 4.85$ A, $C_o = 300$ μF, $C_{\text{bus}} = 5$ μF, $L = 55$ μH and $R_o = 30$ Ω.

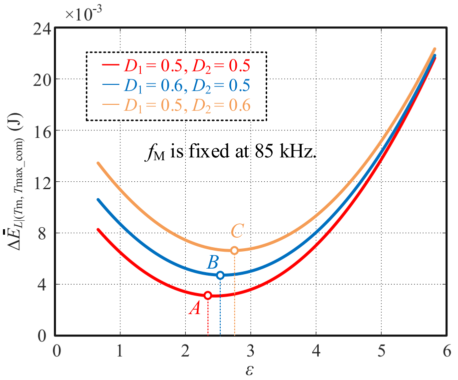

Fig. 18. The energy stored in the inductor during one full-mode period in three operating modes with different ε when $f_M = 85$ kHz and $U_{\text{in}} = U_o = 300$ V.

it is necessary to first determine the value of k_p that achieves the 45° phase margin based on the Bode plots.

Fig. 17 presents the Bode plots of $G_{\text{op\_}E_{\text{bus}}}(s)$ for the small-signal model-based PI controller design, taking the full-mode operating period $f_{\max\_\text{com}} = 1/T_{\max\_\text{com}} = 5$ kHz with the rear-end FSBB converter operating in equal mode as an example. It can be seen from Fig. 17 that when the phase margin of $G_{\text{op\_}E_{\text{bus}}}(s)$ reaches its boundary value of 45°, the proportional coefficient must satisfy the boundary condition $k_p/k_m = -0.5417$. Considering the influence of proportional coefficient k_p on the phase margin demonstrated in Fig. 13(c), it is concluded that the higher phase margins necessitate the larger proportional coefficients, which means that the minimum of k_p/k_m is -0.5417 for the PI controller. With the crossover frequency set to $\omega_c = 10^5$ rad/s ($\omega_c > 3*2\pi f_{\max\_\text{com}}$), the maximum of proportional coefficient k_i/k_m is determined as -13510.6. Thus, for the full-mode energy control strategy of the two-time-scale system, the proportional coefficient k_i/k_m of the PI controller needs to be maintained below -13510.6 to ensure the adequate response speed.

F. Optimization of the Inductor Current

The energy difference between port ($c+$, c-) and port ($d+$, d-) in the unified time scale T_m equals to the energy stored in the inductor L. However, the changes in the inductor current i_L are determined by the energy variations over the period T_N. To reduce the computational errors, it is important to calculate the inductor current based on the energy change in the full-mode operating period $T_{\max\_\text{com}}$. From (15) and (16), the energy variation in $T_{\max\_\text{com}}$ can be given as

$$\Delta\bar{E}_{L|(T_m,T_{\max\_\text{com}})} = \left(E'_{\text{bus}|(T_m,T_{\max\_\text{com}})} - E_{o|(T_V,T_{\max\_\text{com}})}\right) = \sum_{j=1}^{\sigma_M} \left[-\sum_{i=1}^{D_1\sigma_N} X\left(\varsigma_{i,j,},\varsigma_{i-1,j}\right) - \sum_{i=\alpha\sigma_N}^{(\alpha+D_2)\sigma_N} \sigma X\left(\varsigma_{i,j,},\varsigma_{i-1,j}\right) + \sum_{i=1}^{\alpha\sigma_N} Y\left(\varsigma_{i,j,},\varsigma_{i-1,j}\right)\left[\left(D_1^2-\sigma^2 D_2^2\right)+\left(\sigma^2-1\right)\left(D_1-\alpha\right)^2\right] \right] \tag{32}$$

where

$$X\left(\varsigma_{i,j},\varsigma_{i-1,j}\right) = I_{L0}\left[u_{C_{\text{bus}}}\left(\varsigma_{i,j}\right) - u_{C_{\text{bus}}}\left(\varsigma_{i-1,j}\right)\right]T_m$$

$$Y\left(\varsigma_{i,j},\varsigma_{i-1,j}\right) = \frac{1}{2L}\left(\sigma_N T_m\right)^2\left[u^2_{C_{\text{bus}}}\left(\varsigma_{i,j}\right) - u^2_{C_{\text{bus}}}\left(\varsigma_{i-1,j}\right)\right].$$

With the PCCM ZVS modulation in [25], the inductor current I_{L0} in the fourth mode shown in Fig. 4 is limited to I_{L_ZVS}. The RMS value of the inductor current I_{L_RMS} will increase with the energy stored in the inductor, leading to an increase in power losses. Therefore, it is necessary for the rear-end FSBB converter to operate under the condition of the minimum I_{L_RMS}. The average variation of the inductor current $\Delta\langle i_L\rangle$ in the slow-time scale can be obtained as

$$\Delta\langle i_L\rangle_{|(T_m,T_{\max\_\text{com}})} = \left(2\Delta\bar{E}_{L|(T_m,T_{\max\_\text{com}})}/L\right)^{1/2}. \tag{33}$$

It can be observed from (32) and (33) that $\Delta\langle i_L\rangle$ is determined by the energy variations between port ($c+$, c-) and port ($d+$, d-). Thus, the problem of finding the minimum of $\Delta\langle i_L\rangle$ can be equivalently formulated as determining the minimum of the energy variation $\Delta\bar{E}_{L|(T_m,\ T_{\max\_\text{com}})}$.

By applying the Lagrange multiplier optimization method [28], one can obtain the condition for minimizing the port energy difference in the full-mode operating period $T_{\max\_\text{com}}$, which is $D_1 = D_2$ (i.e., $\sigma = 1$).

Fig. 18 illustrates the trend of port energy variations $\Delta\bar{E}_{L|(T_m,\ T_{\max\_\text{com}})}$ in three operating modes versus the time scale ratio ε. It can be observed that when the rear-end FSBB converter operates in the equal mode, $\Delta\bar{E}_{L|(T_m,\ T_{\max\_\text{com}})}$ between ports ($c+$, c-) and ($d+$, d-) is generally lower than in the other two modes, indicating that I_{L_RMS} is minimized at the same operating frequency, which means that the optimal operating mode is $\sigma = 1$ with the PCCM ZVS modulation. Furthermore, the minimum of $\Delta\bar{E}_{L|(T_m,\ T_{\max\_\text{com}})}$, denoted as A, B, and C for the three modes respectively, vary with the operating frequency f_N. Specifically, in the equal mode, $\varepsilon = 2.35$, corresponding to the minimum I_{L_RMS} occurring at the operating frequency of 36.17 kHz. In buck and boost modes, the minimum values are reached at ratios $\varepsilon = 2.532$ and $\varepsilon = 2.764$, respectively, with the corresponding operating frequencies of 33.57 and 30.75 kHz.

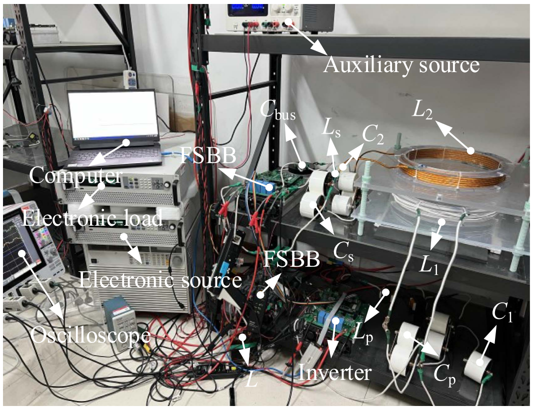

Fig. 19. Experimental prototype.

V. EXPERIMENTAL VERIFICATION

A. Experimental Setup

To validate the performance of the proposed full-mode energy control strategy, an experimental platform including two cascaded stages is built, as shown in Fig. 19. The parameters of the system are listed in Table I. The DSP TMS320F28335 is selected as the controller for control strategy execution and PWM generation. The input and load of the cascaded system are emulated by two ITECH bidirectional dc sources. The power switches Q_{11}~Q_{14}, Q_{21}~Q_{24}, S_1~S_4 are SiC MOSFETs C3M0021120K. The radii of the circular transmitting and receiving coils with 12 turns are both 16 cm. The waveforms are measured by an oscilloscope Tektronix MSO58 8-BW-500.

B. Steady-State Operation

Fig. 20 shows the steady-state waveforms of the two-time-scale cascaded IPT-FSBB system with the full-mode energy control when $\sigma = 1$ and $U_{\mathrm{in}} = 300$ V. To ensure the power transfer ability of the cascaded system, the fast-time-scale IPT system operates at the resonant frequency, which is designed as 85 kHz. By altering the operating frequency of the slow-time-scale FSBB converter, the performance of full-mode energy control strategy conducted in different unified time scales are verified. The ZVS current $-I_{L0}$ of the FSBB converter is set as -4.0 A. In the full-mode period $T_{\mathrm{max\_com}}$, the modulation synchronization is achieved by using the inner phase-shift between the two stages, which has been discussed in [25]. To ensure a fair comparison, the full-mode energy control periods under the three different time scale ratios are uniformly set to 5 kHz.

In Fig. 20(a) and (b), the operating frequency f_{N} in the slow time scale is 20 kHz, the unified time scale can be obtained as $\hat{f}_{m1} = 1/\hat{T}_{m1} = 340$ kHz, and $\sigma_N = 4$. To reduce the RMS value I_{L_RMS} of the inductor current, the slow-time-scale FSBB converter operates in the equal mode (i.e., $\sigma = 1$), the requirements of the output power P_o under different load conditions can be met by adjusting the phase-shift αT_{N}, which is defined as an integer multiple of the unified time scale with the PCCM ZVS modulation. The output power in Fig. 20(a) and (b) are 1.45 and 1.61 kW, respectively. To maintain the operation at the minimum RMS value of the inductor current, the phase-shift αT_N is changed from $2\hat{T}_{m1}$ to $3\hat{T}_{m1}$. Meanwhile, the ZVS operation of the inverter and active rectifier can be realized with the full-mode energy control.

In Fig. 20(c) and (d), the operating frequency f_N in the slow time scale is 45 kHz, the unified time scale can be obtained as $\hat{f}_{m2} = 1/\hat{T}_{m2} = 765$ kHz, and $\sigma_N = 9$. The output powers P_o corresponding to the phase-shifts $\alpha T_N = 2\hat{T}_{m2}$ and $\alpha T_N = 4\hat{T}_{m2}$ are 1.50 kW and 1.59 kW, respectively. As the phase-shift $\alpha_n T_N$ increases, the duration of ZVS current $-I_{L0}$ in the FSBB converter will decrease, which aims to lower the RMS value of the inductor current i_L under the PCCM ZVS modulation strategy.

In Fig. 20(e) and (f), since the operating frequencies of the two stages are identical, the sampling frequency $\hat{f}_{m3} = 1/\hat{T}_{m3}$ is obtained as 850 kHz based on the analysis in Section III, where $\sigma_M = \sigma_N = 10$. The output powers P_o presented in Fig. 20(e) and (f) are 1.40 and 1.49 kW, respectively.

As a result of the full-mode energy control strategy, the phase-shift αT_N is successfully adjusted according to i_o obtained from the two-time-scale energy model. Additionally, as can be observed from Fig. 20, the ripples in the bus capacitor voltage $u_{C\mathrm{bus}}$ decrease with the increase in the operating frequency f_N, indicating that for a given bus capacitance C_{bus}, a larger ε results in a more profound coupling between the two stages of the cascaded system.

C. Dynamic Operation

Fig. 21 shows the dynamic experimental waveforms of the system with the full-mode energy control when the load voltage U_o steps from 300 to 400 V under the input voltage $U_{\mathrm{in}} = 300$ V. In Fig. 21(a), (b), and (c), the sampling frequencies are 340, 765, and 850 kHz, respectively. The full-mode control period is 5 kHz. The adjustment times are 19, 16, and 9 ms, respectively. Within the same control period $T_{\mathrm{max\_com}}$, the increase in the unified time scale $\hat{f}_m$ enhances the two-time-scale energy model's ability to track variations in the output current i_o. Consequently, it leads to a reduction in the adjustment time required by the system to respond to load transients. Meanwhile, under the same output power P_o, the amplitude of the output current ripple increases with the rise in slow time scale f_N. Fortunately, the two-time-scale energy control strategy facilitates a smooth transition of the output current during load transients without any overshoot.

Fig. 22 shows the dynamic response waveforms obtained under the same conditions as those in Fig. 21, but with the application of the single-time-scale energy control, where the fast time scale f_M is selected as both the unified time scale and the control period to ensure the effectiveness of the control strategy. As can be observed from Fig. 22, under the operation of three different time scale ratios, the adjustment times for the single-time-scale energy control method, when the load voltage abruptly changes from 300 to 400 V, are 34, 36, and 31 ms, respectively, which are significantly longer than those achieved by the full-mode energy control based on a two-time-scale model.

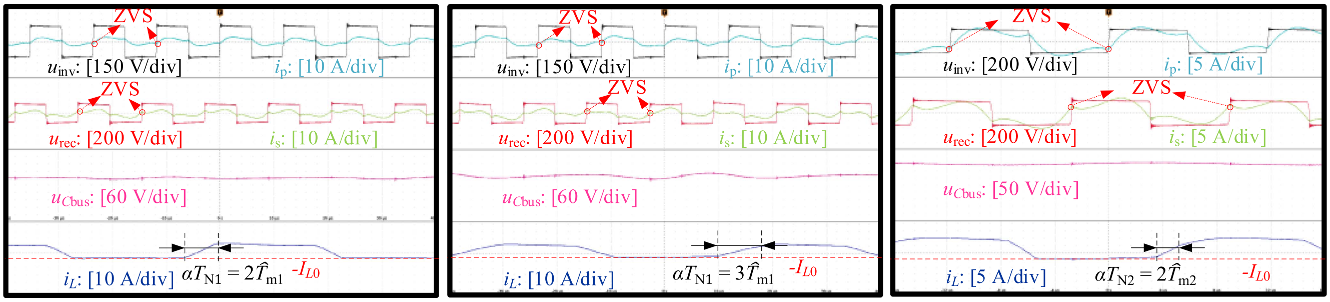

(a) Time: 10 µs/div (b) Time: 10 µs/div (c) Time: 4 µs/div

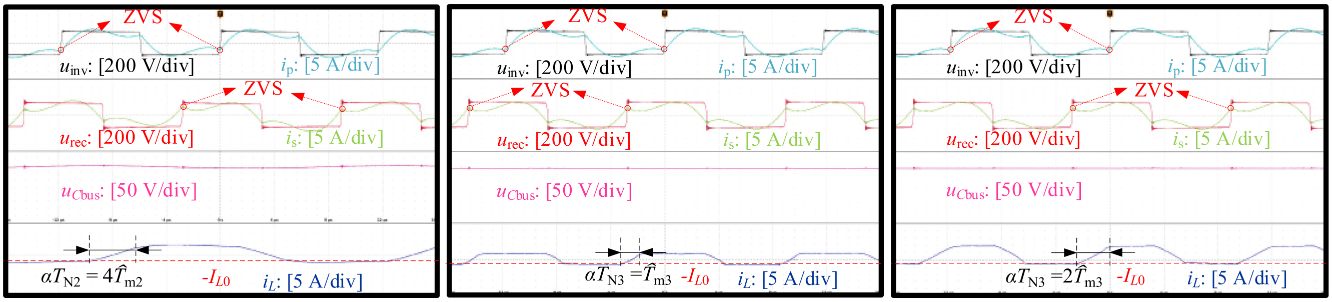

(d) Time: 4 µs/div (e) Time: 4 µs/div (f) Time: 4 µs/div

Fig. 20. Steady-state waveforms with the full-mode energy control when $\sigma = 1$, $U_{\text{in}} = 300$ V, $k_p/k_{mi} = -0.00259$, and $k_i/k_{mi} = -14710.6$. (a) $f_N = 20$ kHz, $\sigma_M = 17$, $\sigma_N = 4$, $\hat{f}_{m1} = 1/\hat{T}_{m1} = 340$ kHz, $P_{\text{o}} = 1.45$ kW. (b) $f_N = 20$ kHz, $\sigma_M = 17$, $\sigma_N = 4$, $\hat{f}_{m1} = 1/\hat{T}_{\text{m1}} = 340$ kHz, $P_{\text{o}} = 1.61$ kW. (c) $f_N = 45$ kHz, $\sigma_M = 17$, $\sigma_N = 9$, $\hat{f}_{m2} = 1/\hat{T}_{m2} = 765$ kHz, $P_o = 1.50$ kW. (d) $f_N = 45$ kHz, $\sigma_M = 17$, $\sigma_N = 9$, $\hat{f}_{m2} = 1/\hat{T}_{m2} = 765$ kHz, $P_o = 1.59$ kW. (e) $f_N = 85$ kHz, $\sigma_M = \sigma_N = 10$, $\hat{f}_{m3} = 1/\hat{T}_{m3} = 850$ kHz, $P_o = 1.40$ kW; (f) $f_N = 85$ kHz, $\sigma_M = \sigma_N = 10$, $\hat{f}_{m3} = 1/\hat{T}_{\text{m3}} = 850$ kHz, $P_o = 1.46$ kW.

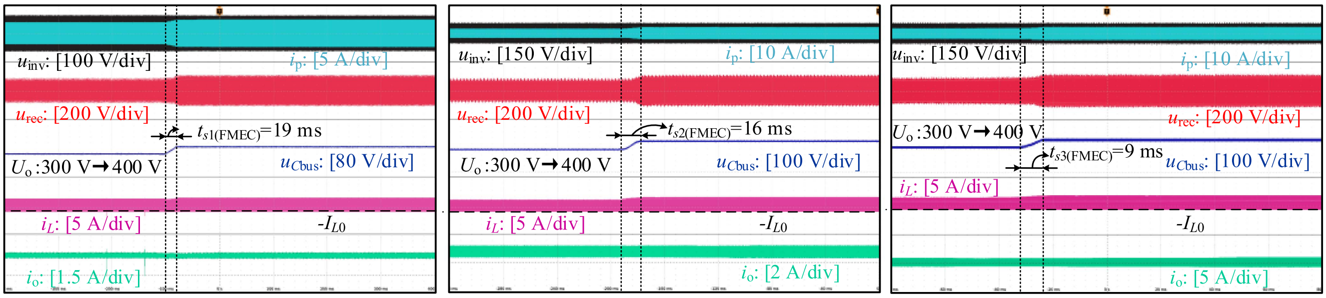

(a) Time: 100 ms/div (b) Time: 40 ms/div (c) Time: 20 ms/div

Fig. 21. Proposed energy control strategy conducted in the full-mode period $T_{\text{max\_com}} = 5$ kHz at load voltage transients when $f_{\text{M}} = 85$ kHz, $\sigma = 1$, $U_{\text{in}} = 300$ V, $k_{\text{p}}/k_{mi} = -0.00259$, and $k_{\text{i}}/k_{mi} = -14710.6$. (a) $f_{\text{N}} = 85$ kHz. (b) $f_{\text{N}} = 45$ kHz. (c) $f_{\text{N}} = 20$ kHz.

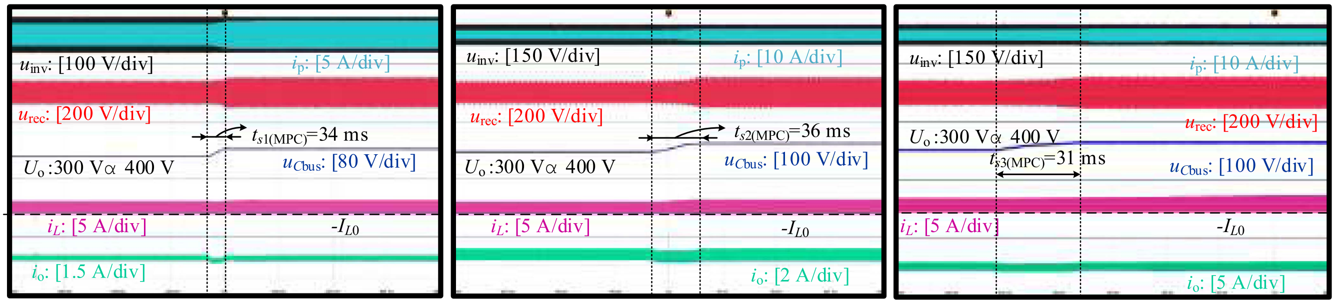

(a) Time: 100 ms/div (b) Time: 40 ms/div (c) Time: 20 ms/div

Fig. 22. Dynamic performance of the cascaded system with single-time-scale energy control at load voltage transients when $f_M = 85$ kHz, $\sigma = 1$, $U_{\text{in}} = 300$ V, $k_p/k_{mi} = -0.00259$, and $k_{\text{i}}/k_{mi} = -14710.6$. (a) $f_{\text{N}} = 85$ kHz, (b) $f_{\text{N}} = 45$ kHz, (c) $f_{\text{N}} = 20$ kHz.

TABLE II
COMPARISON WITH EXISTING CONTROL SCHEMES

Literature	Xiao et al. [11]	Ma et al. [17]	Shan et al. [19]	Liu and Feng [22]	Ma et al. [24]	**This article**
Studied object	IPT-Cuk	DIPT-Buck	Cascaded dc–dc system	IPT system	IPT system	IPT-FSBB
Control strategy	Two-loop control	Model predictive control	Virtual impedance control	Maximum efficiency control	Periodic energy control	Full-mode energy control
Time scales	Two	Two	Multiple	Single	Single	Two
Sampling frequency	Operating frequency	Operating frequency	Operating frequency	Operating frequency	Operating frequency	Unified time scale
Load sampling requirement	Yes	Yes	Yes	Yes	Yes	No
Computational burden	High	Medium	High	Medium	Low	Low
Complexity in software	Medium	Medium	High	Medium	Medium	Low
Complexity in hardware design	High	High	High	Medium	Medium	Low

From Figs. 21 and 22, it can be observed that the two-time-scale energy model demonstrates precise tracking of output current variations during load changes, effectively suppressing undershoot and facilitating smooth transitions between operating modes. In contrast, when applying the single-time-scale energy control across three distinct time-scale ratios ε, the output current consistently shows undershoot. Thus, the full-mode control strategy based on the two-time-scale energy model possesses a more accurate and faster capability to track the system's dynamic response.

D. Comparison and Discussion

Table II compares the proposed full-mode energy control for the two-time-scale cascaded systems with some previous control strategies. The advantages of the proposed method in this article are as follows.

1) Compared to the control strategies in [11], [17], [19], and [22], the proposed method based on the two-time-scale energy model selects the port energy as the control variable. It effectively eliminates the need for integral and exponential calculations, thus addressing the issues of high computational complexity and high sensitivity to parameter identification errors. Moreover, the port energy of the bus capacitor is taken as one of the control variables, which allows the control strategy to adapt to scenarios where the cascaded system is non-fully decoupled.
2) The full-mode energy control strategy employs the unified time scale $\hat{f}_{\mathrm{m}}$ and full-mode operating period $T_{\max\_\mathrm{com}}$ as the sampling frequency and control period, which is capable of accommodating different time-scale ratios, thereby enabling precise tracking of load variations. The constant sampling frequency also facilitates the design of EMI filter. Compared to the periodic energy control in [24], the proposed method can reduce the adjustment time required for cascaded systems to respond to the load changes and effectively mitigates the undershoot phenomenon in load current.
3) The control strategy proposed in this article eliminates the need for sampling load voltage and current, reducing the design complexity and cost of the hardware circuit.

VI. CONCLUSION

To overcome the limitations of the traditional single-time-scale energy model, which fails to accurately track the dynamic response when studying systems with multiple time scales, this article proposes a two-time-scale energy model that offers high accuracy over 98.9%. Furthermore, the full-mode energy control strategy based on the two-time-scale model avoids the need for sampling load voltage and current, effectively reducing the computational burden of the control strategy, which improves the dynamic response speed of the cascaded system during sudden load changes, ensuring a smooth transition of the output current.

REFERENCES

[1] Z. Wang et al., "An optimization approach for efficiency and interoperability enhancement of WPT systems for autonomous underwater vehicles," *IEEE Trans. Power Electron.*, vol. 40, no. 4, pp. 6345–6358, Apr. 2025.
[2] S. Wu, C. Cai, X. Liu, W. Chai, and S. Yang, "Compact and free-positioning omnidirectional wireless power transfer system for unmanned aerial vehicle charging applications," *IEEE Trans. Power Electron.*, vol. 37, no. 8, pp. 8790–8794, Aug. 2022.
[3] K. He, X. Liu, F. Gao, X. Yang, Z. Cheng, and D. Liu, "Accurate discrete-time modeling and boundary analysis for high-order wireless power transfer systems," *IEEE Trans. Power Electron.*, vol. 39, no. 12, pp. 16839–16854, Dec. 2024.
[4] G. Yu, J. Dong, T. B. Soeiro, G. Zhu, Y. Yao, and P. Bauer, "Three-mode variable-frequency ZVS modulation for four-switch buck+boost converters with ultra-high efficiency," *IEEE Trans. Power Electron.*, vol. 38, no. 4, pp. 4805–4819, Apr. 2023.
[5] Y. Huang, N. Shinohara, and T. Mitani, "Impedance matching in wireless power transfer," *IEEE Trans. Micro. Theory Techn.*, vol. 65, no. 2, pp. 582–590, Feb. 2017.
[6] C. Li, Y. Yu, Z. Yang, Q. Liu, and X. Peng, "ESR estimation for aluminum electrolytic capacitor of power electronic converter based on compressed sensing and wavelet transform," *IEEE Trans. Ind. Electron.*, vol. 69, no. 2, pp. 1948–1957, Feb. 2022.
[7] B. Yao, G. Zhu, Q. Wang, H. Wang, and H. Wang, "A noninvasive online evaluation method for core temperature of aluminium electrolytic capacitors," *IEEE Trans. Power Electron.*, vol. 39, no. 3, pp. 2922–2926, Mar. 2024.
[8] H. Hao, G. A. Covic, and J. T. Boys, "An approximate dynamic model of LCL-T-based inductive power transfer power supplies," *IEEE Trans. Power Electron.*, vol. 29, no. 10, pp. 5554–5567, Oct. 2014.
[9] X. Li, X. Ruan, X. Xiong, Q. Jin, and C. K. Tse, "Stability issue of cascaded systems with consideration of switching ripple interaction," *IEEE Trans. Power Electron.*, vol. 34, no. 7, pp. 7040–7052, Jul. 2019.
[10] B. He, W. Chen, H. Mu, D. Zhan, and C. Zhang, "Small-signal stability analysis and criterion of triple-stage cascaded DC system," *IEEE J. Emerg. Sel. Top. Power Electron.*, vol. 10, no. 2, pp. 2576–2586, Apr. 2022.

[11] W. Xiao et al., “Dynamic modeling and control design based on singular perturbation theory for high-order wireless power transfer system,” *IEEE Trans. Ind. Informat.*, vol. 20, no. 5, pp. 7524–7536, May 2024.

[12] A. Kurs, A. Karalis, R. Moffatt, J. D. Joannopoulos, P. Fisher, and M. Soljacic, “Wireless power transfer via strongly coupled magnetic resonances,” *Science*, vol. 317, no. 5834, pp. 83–86, 2007.

[13] H. Li, K. Wang, L. Huang, W. Chen, and X. Yang, “Dynamic modeling based on coupled modes for wireless power transfer systems,” *IEEE Trans. Power Electron.*, vol. 30, no. 11, pp. 6245–6253, Nov. 2015.

[14] S. Assawaworrarit, X. Yu, and S. Fan, “Robust wireless power transfer using a nonlinear parity-time-symmetric circuit,” *Nature*, vol. 546, no. 7658, pp. 387–390, 2017.

[15] J. Zhou, B. Zhang, W. Xiao, D. Qiu, and Y. Chen, “Nonlinear parity-time-symmetric model for constant efficiency wireless power transfer: Application to a drone-in-flight wireless charging platform,” *IEEE Trans. Ind. Electron.*, vol. 66, no. 5, pp. 4097–4107, May 2019.

[16] P. Kokotovic, H. K. Khalil, and J. O’Reilly, “Time-scale modeling,” in *Singular Perturbation Methods in Control Analysis and Design*. Philadelphia, PA, USA: SIAM, 1999, pp. 1–45.

[17] T. Ma, C. Q. Jiang, C. Chen, Y. Wang, J. Geng, and C. K. Tse, “A low computational burden model predictive control for dynamic wireless charging,” *IEEE Trans. Ind. Electron.*, vol. 71, no. 9, pp. 10402–10413, Sep. 2024.

[18] J. Li, M. Yang, F. L. Lewis, and M. Zheng, “Compensator-based self-learning: Optimal operational control for two-time-scale systems with input constraints,” *IEEE Trans. Ind. Informat.*, vol. 20, no. 7, pp. 9465–9475, Jul. 2024.

[19] Z. Shan, S. Fan, X. Liu, X. Ding, and Z. Li, “Transient mitigation using an auxiliary circuit in cascaded DC–DC converter systems with virtual impedance control,” *IEEE Trans. Ind. Electron.*, vol. 69, no. 5, pp. 4652–4664, May 2022.

[20] P. Sun, C. Liu, J.-S. Lai, and C.-L. Chen, “Cascade dual buck inverter with phase-shift control,” *IEEE Trans. Power Electron.*, vol. 27, no. 4, pp. 2067–2077, Apr. 2012.

[21] R. H. Cuzmar, J. Pereda, and R. P. Aguilera, “Phase-shifted model predictive control to achieve power balance of CHB converters for large-scale photovoltaic integration,” *IEEE Trans. Ind. Electron.*, vol. 68, no. 10, pp. 9619–9629, Oct. 2021.

[22] Y. Liu and H. Feng, “Maximum efficiency tracking control method for WPT system based on dynamic coupling coefficient identification and impedance matching network,” *IEEE J. Emerg. Sel. Top. Power Electron.*, vol. 8, no. 4, pp. 3633–3643, Dec. 2020.

[23] S. Lee and S.-H. Lee, “Observer-based online parameter identification of series–series tuned inductive power transfer system,” *IEEE Trans. Ind. Electron.*, vol. 72, no. 3, pp. 2927–2937, Mar. 2025, doi: 10.1109/TIE.2024.3423413.

[24] T. Ma, Y. Wang, X. Hu, D. Zhao, Y. Jiang, and C. Jiang, “Periodic energy control for wireless power transfer system,” *IEEE Trans. Power Electron.*, vol. 37, no. 4, pp. 3775–3780, Apr. 2022.

[25] K. He, F. Gao, X. Liu, Y. Jiang, X. Yang, and D. J. Rogers, “Unified two-time-scale modeling and hybrid ZVS modulation of LCC-LCC compensated IPT system with wide input voltage range,” *IEEE Trans. Power Electron.*, to be published, doi: 10.1109/TPEL.2025.3527508.

[26] W. Zhang and C. C. Mi, “Compensation topologies of high-power wireless power transfer systems,” *IEEE Trans. Veh. Technol.*, vol. 65, no. 6, pp. 4768–4778, Jun. 2016.

[27] B. Litkouhi and H. Khalil, “Multirate and composite control of two-timescale discrete-time systems,” *IEEE Trans. Autom. Control*, vol. 30, no. 7, pp. 645–651, Jul. 1985.

[28] D. Mou, Q. Luo, J. Li, Y. Wei, and P. Sun, “Five-degree-of-freedom modulation scheme for dual active bridge DC–DC converter,” *IEEE Trans. Power Electron.*, vol. 36, no. 9, pp. 10584–10601, Sep. 2021.

[29] G. Zheng, T. Li, X. Wang, and M. Fu, “Stability and controller design of a two-stage inductive power transfer system,” *IEEE Trans. Ind. Electron.*, vol. 72, no. 1, pp. 380–389, Jan. 2025.

[30] K. Li, S.-C. Tan, and R. S. Y. Hui, “On beat frequency oscillation of two-stage wireless power receivers,” *IEEE Trans. Power Electron.*, vol. 35, no. 12, pp. 12741–12751, Dec. 2020.

[31] G. Zheng, P. Zhao, H. Li, and M. Fu, “Small-signal model of an inductive power transfer system using LCC–LCC compensation,” *IEEE Trans Ind. Appl.*, vol. 58, no. 1, pp. 1201–1210, Jan./Feb. 2022.

Kai He (Graduate Student Member, IEEE) received the B.S. degree in electrical engineering from East China University of Science and Technology, Shanghai, China, in 2021. He is currently working toward the Ph.D. degree in electrical engineering with Shanghai Jiao Tong University, Shanghai, China.

His research interests include multiple-time-scale modeling and control of cascaded systems, ZVS modulation of dc–dc converters, and wireless power transfer systems.

Fei Gao (Member, IEEE) received the Ph.D. degree in electrical engineering from the Power Electronics, Machines, and Control (PEMC) Research Group, University of Nottingham, Nottingham, U.K., in 2016.

From March 2010 to September 2012, he has worked in Jiangsu Electric Power Research Institute, Nanjing, State Grid Corporation of China. From 2016 to 2019, he was with Department of Engineering Science, University of Oxford, U.K. as a Postdoctoral Researcher. Since July 2019, he was an Associate Professor with Shanghai Jiao Tong University, Shanghai, China. His current research interests include microgrids, more electric transportation systems and wireless power transfer.

Dr. Gao was the recipient of the European Union Clean Sky Best PhD Award in 2017 and IET Control & Automation Runner Up PhD Award in 2018.

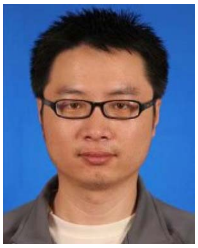

Ying Jiang received the Ph.D. degree in electrical engineer from Shanghai Jiao Tong University, Shanghai, China, in 2011.

Since 2011, he has been an Associate Professor with Shanghai Dianji University, Shanghai, China. His current research interests include power electronics magnetic integration, wireless power transfer and more electric transportation systems.

Xijun Yang (Member, IEEE) received the Ph.D. degree in control engineering from Shanghai University, Shanghai, China, in 2002.

From 1992 to 1995, he was an Electrical Engineer with Handan Institute of Coal Mine Design and Research, Hebei, China. From 2013 to 2014, he was a Guest Associate Professor with the Department of Energy Technology, Aalborg University, Aalborg, Denmark. From 2004 to 2013, he was with the Department of Electrical Engineering, Shanghai Jiao Tong University, where since 2014, he has been an Associate Professor. His current research interests include wireless power transfer, power conversion, and solid state transformers.

Hongchen Liu (Senior Member, IEEE) received the B.S. degree from Northeast Agricultural University, Harbin, China, in 2001, and the master’s and Ph.D degrees from Harbin Institute of Technology (HIT), Harbin, China, in 2003 and 2007, respectively, all in electrical engineering.

In 2009, he was a Lecturer with the Department of Electrical Engineering, HIT, where he has been a Professor of electrical engineering since 2020. He has authored more than 120 technical papers published in journals and conference proceedings. His current major research interests include dc–dc converter and inverter in photovoltaic system, Matrix converter, and nonlinear dynamics in power electronics.